國立臺灣大學理學院物理學研究所
碩士論文
Department of Physics
College of Science
National Taiwan University
Master's Thesis

Belle II 實驗中 $B^{\pm} \to \omega K^{\pm}$ 與 $B^{\pm} \to \omega \pi^{\pm}$ 衰變的分支比與直接 CP 不對稱性測量

Measurement of Branching Fractions and Direct CP Asymmetries for $B^{\pm} \to \omega K^{\pm}$ and $B^{\pm} \to \omega \pi^{\pm}$ Decays at Belle II

徐舟晗
ZhouHan Xu

指導教授：張寶棣 博士
Advisor: Pao-Ti Chang, Ph.D.

中華民國 114 年 7 月
July, 2025

doi:10.6342/NTU202504255

國立臺灣大學碩士學位論文
口試委員會審定書
MASTER'S THESIS ACCEPTANCE CERTIFICATE
NATIONAL TAIWAN UNIVERSITY

（論文中文題目）(Chinese title of Master's thesis)

Belle II 实验中 $B^{\pm} \to \omega K^{\pm}$ 和 $B^{\pm} \to \omega \pi^{\pm}$ 衰变的分支比及直接 CP 不对称性测量

（論文英文題目）(English title of Master's thesis)

Measurement of Branching Fraction and Direct CP Asymmetries for $B^{\pm} \to \omega K^{\pm}$ and $B^{\pm} \to \omega \pi^{\pm}$ Decays at Belle II

本論文係 徐舟晗 (姓名) R10222086 (學號) 在國立臺灣大學 物理系物理班 系/所/學位學程)完成之碩士學位論文，於民國 114 年 7 月 30 日承下列考試委員審查通過及口試及格，特此證明。

The undersigned, appointed by the Department / Institute of physics on 30 (date) 7 (month) 2025 (year) have examined a Master's thesis entitled above presented by ZHOUHAN XU (name) R10222086 (student ID) candidate and hereby certify that it is worthy of acceptance.

口試委員 Oral examination committee:

張寶棣	張敏娟	趙元
（指導教授 Advisor）		
王名儒		

Acknowledgements

时光荏苒，转眼间我初入台湾大学物理系的那一刻，已化作充满挑战与成长的四年旅程。刚踏入象牙塔时，我满怀对理论物理的憧憬，然而随着学习的深入，也逐渐体会到那片领域对“天赋与勤奋”双重要求的严苛。正当我迷茫之际，一次偶然的机会将我引向台大高能物理实验组，从此开启了Belle II实验的探究之路。

首先，我要衷心感谢我的导师——张宝棣教授。感谢您在我对实验物理尚不熟悉、编程与分析技术尚待磨砺之时，给予我最大程度的包容与支持。无论是在物理分析上为我指点迷津，还是在各类脚本调试中耐心解答，您始终以严谨治学的态度和温暖宽厚的胸怀，引领我一步步走出困惑、攻克难题，使我得以顺利完成本篇硕士论文。

我还要感谢实验室的每一位同门与师兄师姐。您们无私分享Belle II数据处理、粒子鉴别与模拟工具的使用心得，让我在学习过程中少走了许多弯路；您们对我代码调试时的建议和对物理问题的探讨，无不让我深刻体会到团结协作、互助互学的学术氛围。特别感谢李清化、陈文、张传学长姐们，以及陈彦宇，陈劲豪，谢侑澄，陈玮承等等，在生活与研究上的关怀与鼓励，使得艰难的实验日常也充满了欢声笑语。

同时，我要感谢Belle II国际合作组的所有同仁，包括位于KEK与DESY的工程师和技术人员，及背后默默支持数据存储与计算资源的工作人员。感谢CAMPAIGN经费与中央研究院、科技部等机构对本研究项目的资金资助，让实验得以顺利开展。

更要感谢我的家人：即使在我最糟糕的时候，我的父母和家人们也没有放弃我，一直给我无限的支持。

至此，我将满怀感激之情，继续以严谨的学术态度和永不止步的好奇心，投身未来的科研道路。谢谢你们，见证并成就了我的成长。

Time flies, and in the blink of an eye, the moment I first entered the Department of Physics at National Taiwan University has turned into a four-year journey full of challenges and growth. When I first stepped into the academic world, I was filled with admiration for theoretical physics. However, as my studies deepened, I gradually realized the demanding requirements of both talent and perseverance in that field. At a time when I felt lost, a chance opportunity led me to the High Energy Physics Experimental Group at NTU, opening the door to my exploration of the Belle II experiment.

First and foremost, I would like to express my heartfelt gratitude to my advisor, Professor Pao-Ti Chang. Thank you for your utmost patience and support when I was

doi:10.6342/NTU202504255

still unfamiliar with experimental physics and in need of sharpening my programming and analysis skills. Whether guiding me through the intricacies of physics analysis or patiently helping me debug various scripts, you have always led me with your rigorous academic attitude and warm, generous spirit, enabling me to overcome difficulties step by step and successfully complete this master's thesis.

I am also grateful to every fellow lab member and senior colleague. Your selfless sharing of experience in Belle II data processing, particle identification, and simulation tools saved me from many detours. Your advice during code debugging and discussions on physics problems have allowed me to truly experience the spirit of teamwork, mutual assistance, and collaborative learning. Special thanks to Li Qinghua, Chen Wenxu, Zhang Chuanyu, as well as Chen Yanyu, Chen Jinghao, Hsieh You-Cheng, and Chen Weicheng, among others, for your care and encouragement in both life and research, making the challenging days of experimental work full of laughter.

At the same time, I wish to thank all members of the Belle II international collaboration, including engineers and technical staff at KEK and DESY, and those who quietly support the data storage and computing resources. I also appreciate the funding from the CAMPAIGN project, Academia Sinica, the Ministry of Science and Technology, and other institutions, which made this research possible.

Most importantly, I thank my family: even in my most difficult times, my parents and relatives never gave up on me, always giving me unconditional support.

With gratitude in my heart, I will continue to devote myself to future scientific research with a rigorous academic attitude and an unceasing curiosity. Thank you for witnessing and contributing to my growth.

doi:10.6342/NTU202504255

摘要

我们报告了基于详尽的蒙特卡洛模拟衰变模型，对无味强子衰变$B^+ \to \omega K^+$和$B^+ \to \omega\pi^+$的支分数及直接CP电荷不对称性进行可行性研究的结果。
此模拟采用完整的LS1探测器几何结构和响应，针对$\Upsilon(4S)$共振下相当于362 fb^{-1}的数据量（约$(387 \pm 1) \times 10^6$对$B\bar{B}$）。$\omega \to \pi^+\pi^-\pi^0$末态通过基于事件形状和运动学特征训练的多变量分类器进行重建，以优化信号选择并抑制连续体背景。信号产额通过对束约束质量M_{bc}和能量差ΔE的无分箱扩展极大似然拟合提取。我们评估支分数在10^{-6}量级的统计精度，并预计CP不对称灵敏度达百分数水平。
我们从控制信道$B^+ \to \bar{D}^0\pi^+$样本中逐事件提取数据对MC的校正因子，校正跟踪效率、PID及分类器性能，以降低系统偏差并增强灵敏度预测。
最终结果将在未来Belle II实际数据去盲后给出。本研究验证了分析策略，并表明我们已做好应对即将到来数据集的准备。

关键字：Belle II，蒙特卡洛模拟，无味 B 衰变，ω 介子，支分数预测，CP不对称灵敏度，去盲

doi:10.6342/NTU202504255

Abstract

We report feasibility studies of branching fractions and direct CP-violating charge asymmetries in the charmless hadronic decays $B^+ \to \omega K^+$ and $B^+ \to \omega \pi^+$ based on detailed Monte Carlo simulations of our decay model.

The simulation uses the full LS1 detector geometry and response corresponding to 362 fb^{-1} at the $\Upsilon(4S)$ resonance, equivalent to $(387 \pm 1) \times 10^6$ $B\bar{B}$ pairs. Final states with $\omega \to \pi^+\pi^-\pi^0$ are reconstructed using a multivariate classifier trained on event-shape and kinematic features to optimize signal selection and suppress continuum backgrounds. Signal yields are extracted via unbinned extended maximum-likelihood fits to the beam-constrained mass $M_{\rm bc}$ and energy difference ΔE. We assess the expected statistical precision on branching fractions at the 10^{-6} level and project sensitivity to CP asymmetries at the few-percent level.

We derive event-by-event data-to-MC scale factors from control-channel $B^+ \to \bar{D}^0\pi^+$ samples—correcting tracking, PID, and classifier performance—to reduce systematic biases and strengthen our sensitivity projections.

Final results will be obtained upon unblinding of real data in future Belle II analyses. These studies validate our analysis strategy and demonstrate readiness for the upcoming dataset.

Keywords: Belle II, Monte Carlo simulation, charmless B decays, ω meson, branching fraction projection, CP asymmetry sensitivity, unblinding

doi:10.6342/NTU202504255

Contents

doi:10.6342/NTU202504255

doi:10.6342/NTU202504255

doi:10.6342/NTU202504255

List of Figures

doi:10.6342/NTU202504255

doi:10.6342/NTU202504255

List of Tables

doi:10.6342/NTU202504255

Chapter 1

Introduction

1.1 Standard Model

The Standard Model (SM) give us a unified description of all known elementary particles (see Fig. 1.1) and the electromagnetic, weak, and strong forces that govern their interactions. It is a mathematically consistent theory that has been rigorously tested and confirmed by experiments, successfully predicting phenomena ranging from electroweak symmetry breaking to hadron spectroscopy. However, several fundamental questions remain unanswered. For example, the SM cannot fully account for the observed matter–antimatter imbalance in the universe. Although it includes CP violation—a necessary ingredient for baryogenesis—the amount of CP violation in SM processes is far too small to generate the baryon asymmetry we observe today. Moreover, the SM offers no explanation for dark matter, neutrino masses, or the incorporation of gravity, indicating the need for new physics beyond its current framework [1].

1.2 CP Violation in SM

In the Standard Model, CP violation arises solely from a single irreducible complex phase in the Cabibbo–Kobayashi–Maskawa (CKM) matrix [2][3], which relates quark

doi:10.6342/NTU202504255

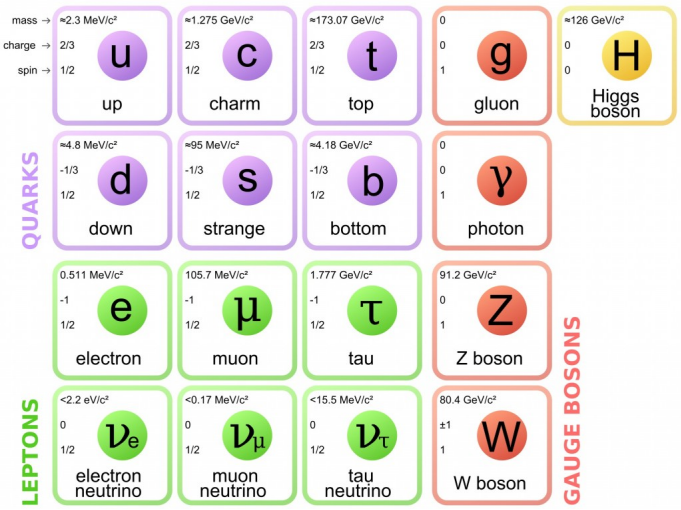

Figure 1.1: Elementary particles of the SM.

mass eigenstates to weak interaction eigenstates:

$$\begin{pmatrix} d' \\ s' \\ b' \end{pmatrix} = \begin{pmatrix} V_{ud} & V_{us} & V_{ub} \\ V_{cd} & V_{cs} & V_{cb} \\ V_{td} & V_{ts} & V_{tb} \end{pmatrix} \begin{pmatrix} d \\ s \\ b \end{pmatrix}. \tag{1.1}$$

By extending the Glashow–Iliopoulos–Maiani mechanism [4] to include a third generation of quarks (top t and bottom b), Kobayashi and Maskawa demonstrated that this phase leads to observable CP-violating effects in weak decays. These effects appear as:

- *Indirect CP violation* in neutral meson mixing, e.g. $K^0 - \overline{K}^0$ and $B^0 - \overline{B}^0$ oscillations.
- *Direct CP violation* in decay-rate asymmetries between a process and its CP-conjugate.

Unitarity of the CKM matrix implies orthogonality relations such as

$$V_{ud}V_{ub}^* + V_{cd}V_{cb}^* + V_{td}V_{tb}^* = 0, \tag{1.2}$$

doi:10.6342/NTU202504255

which can be represented as the Unitarity Triangle in the complex plane. Its internal angles (α, β, γ) are directly measured through CP asymmetries in B-meson decays.

A commonly used parameterization is the Wolfenstein expansion (λ, A, ρ, η), where the CP-violating phase is encoded in η. The overall magnitude of CP violation in the quark sector is characterized by the Jarlskog invariant,

$$J = \Im\left[V_{ud}V_{cs}V_{us}^{*}V_{cd}^{*}\right], \tag{1.3}$$

which vanishes if and only if there is no CP violation.

1.3 Charmless B decays and Direct CP Violation

Charmless hadronic B-meson decays, in which no charm quarks appear in the final state, typically exhibit very small branching fractions, on the order of $\mathcal{O}(10^{-5})$ or below. Such suppression arises from two primary mechanisms. First, many of these final states can only be accessed via the tree-level $b \to u$ transition, which is highly suppressed by the small magnitude of the Cabibbo–Kobayashi–Maskawa (CKM) matrix element $|V_{ub}|$. Second, a large fraction of these decays proceed through loop (penguin) diagrams, which are further suppressed by the loop factor and CKM hierarchies.

Despite their rarity, charmless hadronic decays provide an excellent environment to search for and study direct CP violation. This is because the dominant decay amplitude is usually small, allowing a second amplitude with a different CKM phase to be of comparable magnitude. When the two amplitudes also acquire a non-negligible strong (hadronic) phase difference, their interference can generate sizable direct CP-violating effects. Indeed, several charmless B-meson decay channels have already exhibited clear signatures of direct CP violation in previous B-factory experiments.

The landscape of potentially interesting decay modes is vast. Considering only (quasi) two-body final states where both mesons belong to the ground-state pseu-

doi:10.6342/NTU202504255

doscalar or vector nonets, there are approximately 130 possible channels. The number of accessible modes increases dramatically when including three-body decays, excited meson states, or more exotic hadronic final states. With its high integrated luminosity and advanced detector capabilities, the Belle II experiment is expected to substantially extend the knowledge of these charmless hadronic B decays, enabling precision measurements of branching fractions and CP-violating observables.

From a theoretical perspective, these decays are conveniently described within the framework of the low-energy effective weak Hamiltonian, which incorporates short-distance physics through Wilson coefficients and long-distance hadronic effects in the form of matrix elements of local four-quark operators. This approach allows one to systematically analyze tree and penguin contributions, as well as their interference patterns, which play a crucial role in generating observable CP asymmetries.

These decays are effectively described by the Hamiltonian

$$\mathcal{H}_{\text{eff}} = \frac{G_F}{\sqrt{2}} \left\{ \sum_{q=u,c} V_{qb} V_{qd}^* \Big[C_1(\mu) O_1^q(\mu) + C_2(\mu) O_2^q(\mu) \Big] - V_{tb} V_{td}^* \sum_{i=3}^{10} C_i(\mu) O_i(\mu) \right\} + \text{h.c.} \tag{1.4}$$

which separates the short-distance dynamics (encoded in the Wilson coefficients C_i) from the long-distance QCD effects in the four-quark operators O_i. The decay amplitude can be written as $A = T\, e^{i\delta_T}\, e^{i\phi_T} + P\, e^{i\delta_P}\, e^{i\phi_P}$, where T and P are the magnitudes of the tree and penguin contributions, δ_T and δ_P are the strong phases due to QCD effects, and ϕ_T and ϕ_P are the weak phases from the CKM matrix. Direct CP violation arises when there is interference between these amplitudes, with the CP asymmetry being proportional to . For neutral B mesons decaying to CP eigenstates, mixing-induced CP violation is observed in the time-dependent decay rate $\sin(\delta_P - \delta_T) \sin(\phi_P - \phi_T)$ For neutral B mesons decaying to CP eigenstates, mixing-induced CP violation is observed in the time-dependent decay rate

doi:10.6342/NTU202504255

$$\Gamma(B^0(t) \to f_{CP}) \propto e^{-\Gamma t}\,[1 + S_f\,\sin(\Delta m\,t) - C_f\,\cos(\Delta m\,t)] \qquad (1.5)$$

where $S_f = \frac{2\,\mathrm{Im}(\lambda_f)}{1+|\lambda_f|^2}$, $C_f = \frac{1-|\lambda_f|^2}{1+|\lambda_f|^2}$ and $\lambda_f = e^{-2i\beta}\,\frac{\bar{A}_f}{A_f}$ with β being an angle of the CKM unitarity triangle. Different decay modes, such as $B \to \pi\pi$ and $B \to K\pi$, exhibit varying degrees of tree and penguin contributions, making them powerful probes for testing CP violation within the Standard Model and for revealing potential new physics.

1.4 Motivation

Two body charmless hadronic B decays are interesting for the search for CP violation and test of current understandings of B decay

There also exists a notable mismatch between the predicted and measured CP asymmetries in the $B^{\pm} \to \omega K^{\pm}$ decay. Theoretical estimates based on QCD factorization [5], perturbative QCD factorization [6], and soft collinear effective theory [7] yield values of $0.221^{+0.137+0.140}_{+0.128-0.130}$, $0.32^{+0.15}_{-0.17}$, and $0.116^{+0.182+0.011}_{-0.204-0.011}$, respectively. Despite considerable uncertainties in these approaches, they consistently predict a significant CP asymmetry for this decay. In contrast, experimental data from Belle [8] and BaBar [9] show an asymmetry close to zero, with a latest world average of $ACP = -0.02 \pm 0.04$ on PDG. The current theoretical models have not yet resolved this discrepancy.

In this research we are going to measure the branching ratios of decays and CP asymmetry , compare to the previous measurement in Belle The comparison of the results with CLEO ,BaBar and Belle are summarized in the table :

In this research we are going to measure the branching ratios of decays and CP asymmetry , compare to the previous measurement in Belle The comparison of the results with CLEO ,BaBar and Belle are summarized in the table 1.1 and 1.2.

In this analysis, the branching fraction and direct CP asymmetry of the signal

doi:10.6342/NTU202504255

	Belle (10^{-6})	**BaBar** (10^{-6})	**CLEO II** (10^{-6})	**PDG average** (10^{-6})
$\mathrm{Br}(B^+ \to \omega K^+)$	$6.8 \pm 0.4 \pm 0.4$	$6.3 \pm 0.5 \pm 0.3$	$3.2^{+2.4}_{-1.9} \pm 0.8$	6.5 ± 0.4
$\mathrm{Br}(B^+ \to \omega \pi^+)$	$6.7 \pm 0.5 \pm 0.4$	$6.9 \pm 0.6 \pm 0.5$	$11.3^{+3.3}_{-2.9} \pm 1.4$	6.9 ± 0.5

Table 1.1: Branching fractions measured by Belle, BaBar, CLEO II and the PDG average.

	Belle	**BaBar**	**CLEO II**	**LHCb**	**PDG average**
$\mathbf{Acp}(B^+ \to \omega K^+)$	$-0.03 \pm 0.04 \pm 0.01$	$-0.01 \pm 0.07 \pm 0.01$	No data	No data	-0.02 ± 0.04
$\mathbf{Acp}(B^+ \to \omega \pi^+)$	$-0.02 \pm 0.08 \pm 0.01$	$-0.02 \pm 0.09 \pm 0.01$	-0.34 ± 0.25	$-0.048 \pm 0.065 \pm 0.038$	-0.04 ± 0.05

Table 1.2: Direct CP asymmetry measurements of $B^+ \to \omega K^+$ and $B^+ \to \omega \pi^+$.

B decay are extracted simultaneously via an unbinned maximum-likelihood fit in the three-dimensional space spanned by ΔE, M_{bc}, and $\mathcal{H}_\omega$. Here, $\Delta E = E_{\mathrm{beam}} - E_B$ is the difference between the nominal beam energy and the reconstructed B candidate energy, $M_{bc} = \sqrt{E^2_{\mathrm{beam}} - |\vec{p}_B|^2}$ is the beam-energy–constrained mass, and $\mathcal{H}_\omega$ denotes the helicity angle of the daughter ω meson, which follows a characteristic polarization distribution. Prior to unblinding the Belle II Run 1 data, we optimized the full analysis chain—including track and photon reconstruction, candidate selection, and fit configuration—using large Monte Carlo samples. The fit performance and potential biases in the simultaneous extraction were then evaluated through extensive pseudo-experiment studies, linearity tests over a range of injected asymmetries and branching fractions, and a partial unblinding procedure to validate the robustness of the results.

doi:10.6342/NTU202504255

Chapter 2

Belle II Experiment

Belle II [10] is the world's first Super B-Factory, built to perform precision studies of weak-interaction parameters and to search for New Physics beyond the Standard Model. Situated in Tsukuba, Ibaraki, Japan, it began operation in 2019 and has since collected an integrated luminosity of $362\,\mathrm{fb}^{-1}$ at the $\Upsilon(4S)$ resonance. In June 2022, SuperKEKB set a new record for instantaneous luminosity of approximately $4.7 \times 10^{-34}\,\mathrm{cm}^{-2}\mathrm{s}^{-1}$. After an extended shutdown for accelerator and detector upgrades, data taking resumed in 2024, and by December 2024 achieved $5.1 \times 10^{34}\,\mathrm{cm}^{-2}\mathrm{s}^{-1}$, corresponding to a total dataset of $575\,\mathrm{fb}^{-1}$ (Fig. 2.1).

Compared with its predecessor, KEKB and the Belle detector [11], Belle II incorporates several major improvements: a new six-layer vertex detector, an enhanced central tracking system, and a high-resolution particle identification system. These upgrades deliver superior vertex resolution, increased tracking efficiency, and better separation of particle species—capabilities that are crucial for precision measurements of CP violation and the study of rare decays. By exploiting these advances, Belle II offers an unparalleled experimental environment to test the Standard Model and uncover possible hints of New Physics.

doi:10.6342/NTU202504255

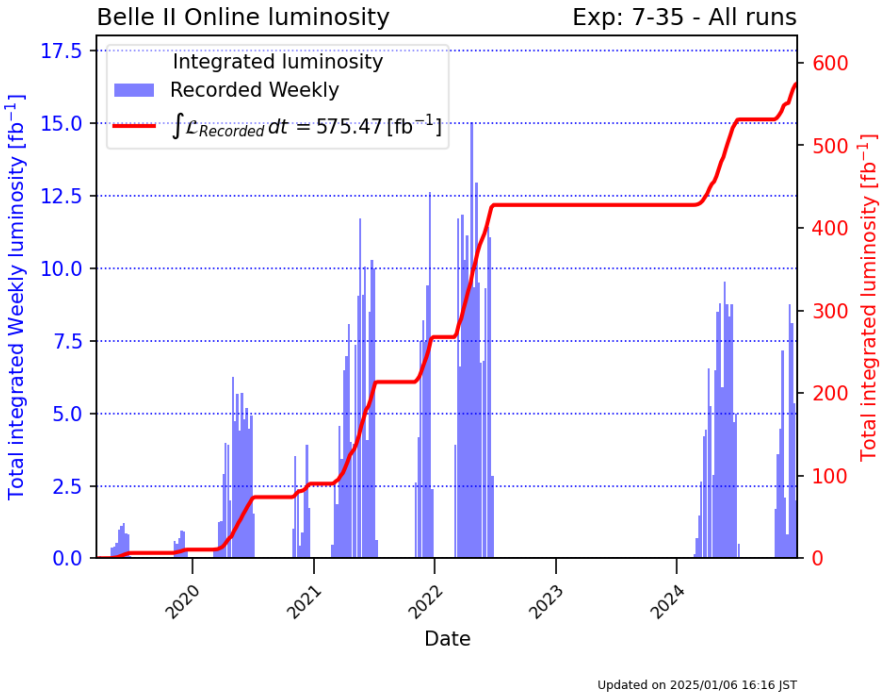

Figure 2.1: Total recorded integrated luminosity up to now.

2.1 SuperKEKB Accelerator

SuperKEKB [12] is an asymmetric-energy e^+e^- collider at KEK, Japan, featuring two storage rings: the High Energy Ring (HER) for 7GeV electrons and the Low Energy Ring (LER) for 4GeV positrons. The beams intersect at an angle of 83mrad, yielding a center-of-mass energy $\sqrt{s} = 10.58$ GeV/c^2, just above the $B\bar{B}$ production threshold of the $\Upsilon(4S)$ resonance. This setup produces B mesons that are nearly at rest in the center-of-mass frame, providing a clean sample of B^+B^- and $B^0\bar{B}^0$ pairs.

To reach its design luminosity of $8 \times 10^{35}\,\mathrm{cm}^{-2}\mathrm{s}^{-1}$, SuperKEKB uses a nano-beam collision scheme with extremely small beam sizes at the interaction point and runs at high beam currents, improving performance by roughly an order of magnitude over KEKB. The energy asymmetry imparts a Lorentz boost of $\beta\gamma \approx 0.28$, which enables spatial separation of the two B decay vertices for time-dependent CP-violation measurements.

doi:10.6342/NTU202504255

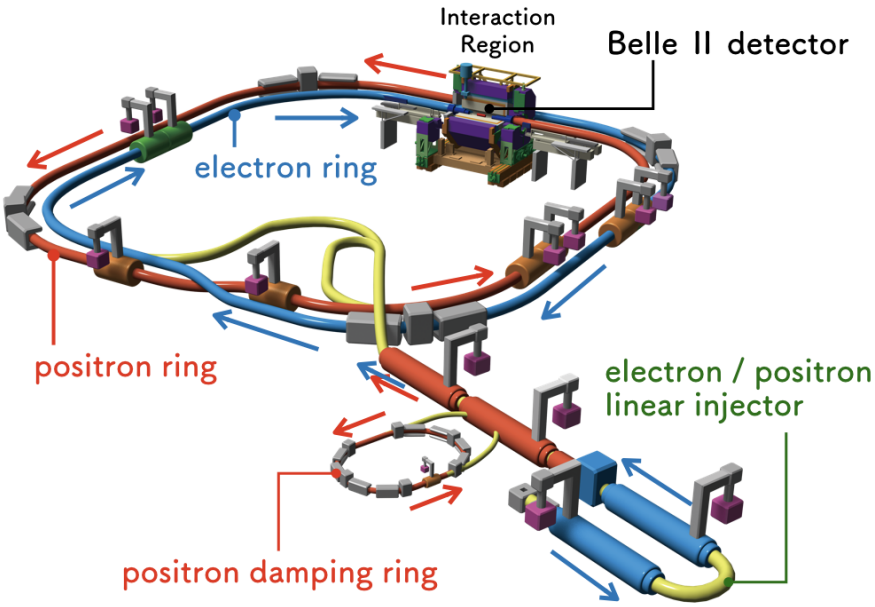

Figure 2.2: SuperKEK accelerator.

2.2 Belle II Detector

2.2.1 Particle Identification System (TOP and ARICH)

For particle identification in the barrel region, a time-of-propagation (TOP) counter is used [13]. This Cherenkov detector measures each photon's arrival time and impact position at the photo-detector located at one end of a 2.6 m quartz bar (2.3). Sixteen identical modules each consist of a 45 cm × 2 cm quartz bar with a 10 cm expansion wedge at the sensor end. The wedge provides a simple pinhole image, eases timing precision requirements, and lowers hit occupancy on the detector. At its exit, two rows of sixteen fast multi-anode sensors (16-channel MCP-PMTs) record photons with 100 ps single-photon resolution, enabled by custom waveform-sampling read-out electronics.

In the forward end-cap, a proximity-focusing RICH (ARICH) uses aerogel radiators to identify charged particles from 0.4 GeV/c to 4 GeV/c. Two 2 cm aerogel layers (n = 1.045 upstream, n = 1.055 downstream) boost photon yield without degrading angle resolution (2.3). A 73×73 mm^2, 144-channel hybrid avalanche photon

doi:10.6342/NTU202504255

detector (HAPD)—developed with Hamamatsu—accelerates photoelectrons over 8 kV onto APDs for single-photon detection.

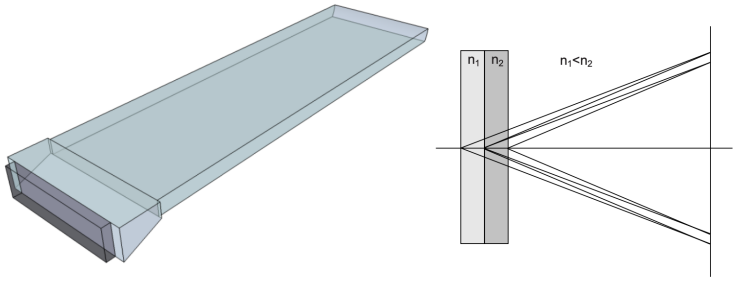

Figure 2.3: Belle II particle-identification subsystems: (left) a single module of the TOP counter; (right) schematic of the proximity-focusing RICH using a gradient-index aerogel radiator in its focusing arrangement.

2.2.2 Vertex detector

The Belle II vertex detector integrates two subsystems—the DEPFET-based Pixel Detector (PXD) and the strip-based Silicon Vertex Detector (SVD)—into six concentric layers surrounding a 10mm–radius beryllium beam pipe 2.4. The two innermost layers at $r = 14$mm and $r = 22$mm employ ultra-thin DEPFET pixel sensors, offering high signal-to-noise ratios and minimal material budget [14, 15]. The four outer layers, located at radii of 38mm, 80mm, 115mm, and 140mm, are built from double-sided silicon strip modules with stereo segmentation to provide precise three-dimensional hit information. Relative to the original Belle detector, the beam pipe and first two sensor layers have been moved significantly closer to the interaction point, while the outermost layer is positioned at a larger radius. These design choices reduce multiple-scattering effects and improve both transverse and longitudinal impact-parameter resolutions (down to $\sim 15\mu$m in the transverse plane), leading to enhanced vertex-finding capability and a higher reconstruction efficiency for short-lived decays such as $K^0_S \to \pi^+\pi^-$ with hits in the vertex detector [16].

doi:10.6342/NTU202504255

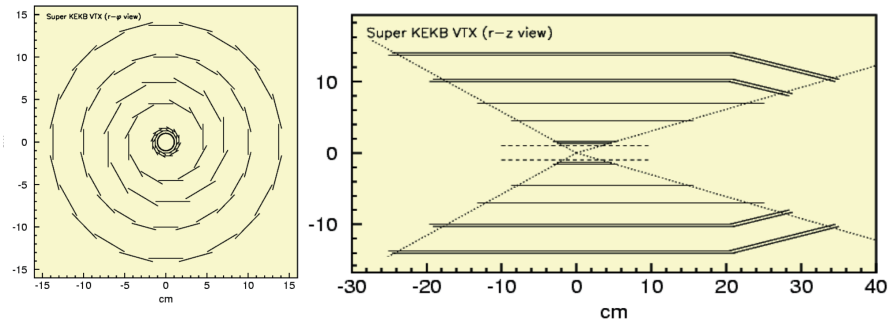

Figure 2.4: A schematic illustration of the Belle II vertex detector, featuring a beryllium beam pipe encircled by two pixel-sensor layers and four silicon-strip-sensor layers.

2.2.3 K_L and μ Detector

The KLM (K-long and Muon) detector sits in the outermost layer of Belle II and serves two main purposes: tagging highly penetrating muons and detecting long-lived neutral K-longs[17]. It alternates iron absorber plates—which guide the return flux of the solenoid field, stop soft backgrounds, and capture K-long decay products with active detector layers.

To handle the intense luminosity and backgrounds at SuperKEKB, the barrel uses resistive-plate chambers (RPCs), while the endcaps employ plastic scintillator modules with embedded wavelength-shifting fibers read out by silicon photomultipliers (SiPMs). This combination boosts both detection efficiency and noise immunity, and—with a shorter event window—reduces false triggers, sharpening the spatial and timing resolution for muon and K-long identification.

2.2.4 Central Drift Chamber

One of the key components of the Belle II spectrometer is the central drift chamber (CDC), a large-volume tracking detector with finely segmented drift cells. Compared with its predecessor in Belle, the CDC has an increased outer radius (1130 mm versus 880 mm), enabled by the use of a thinner barrel particle-identification device. To cope with higher event rates and elevated background conditions, the chamber is

doi:10.6342/NTU202504255

built with smaller drift cells than those in the original Belle detector.

The CDC consists of 14336 sense wires arranged in 56 layers, oriented either *axially* (parallel to the solenoidal magnetic field) or in *stereo* configuration (slightly skewed with respect to the axial wires). By combining information from the axial and stereo layers, complete three-dimensional helical tracks can be reconstructed. The chamber is filled with a 50:50 gas mixture of He and C_2H_6, providing an average drift velocity of 3.3 cm/μs and a maximum drift time of approximately 350 ns for the 17 mm cell size. The CDC has been fully constructed, installed in the Belle II detector, and successfully commissioned using cosmic-ray data (Fig. 2.5).

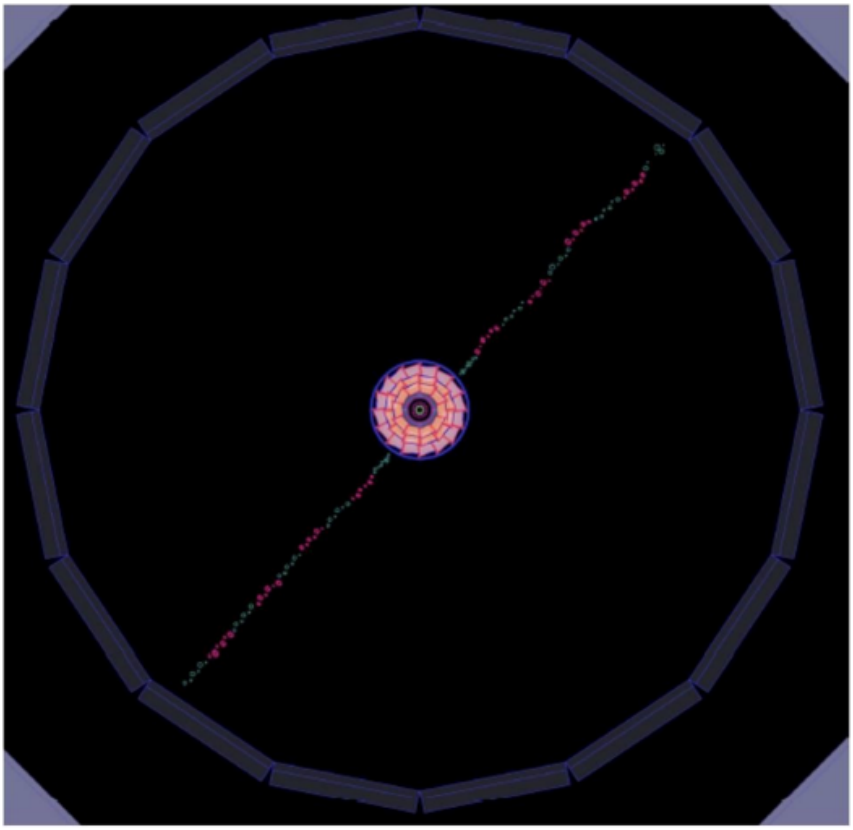

Figure 2.5: Cosmic-muon event recorded in the Belle II Central Drift Chamber.

doi:10.6342/NTU202504255

2.2.5 Electromagnetic Calorimeter

The electromagnetic calorimeter is responsible for photon detection (γ) and electron identification, enabling clear discrimination between electrons and hadrons (notably pions)[18]. It is constructed from a projectively arranged, finely segmented array of CsI crystals[19]. The barrel, forward, and backward end-cap regions together contain 8736 crystals, covering roughly 90% of the solid angle in the center-of-mass frame.

2.2.6 Trigger

The Belle II trigger system employs a two-tiered architecture to efficiently sift through the enormous flux of e^+e^- collisions.[20] The first stage is the Level-1 (L1) hardware trigger, which comprises several specialized sub-triggers: – The Central Drift Chamber (CDC) track trigger identifies high-p_T tracks.[21] – The Electromagnetic Calorimeter (ECL) energy trigger flags large energy deposits.[22] – The KLM system tags penetrating muons and neutral hadrons.[22] – The TOF/TOP system contributes precise timing information for particle identification.[22] Each sub-trigger issues a request to the Global Decision Logic (GDL), where a predefined trigger menu is applied. Within roughly 5 μs, the GDL combines these requests and issues an L1 Accept, with a design rate of up to 30 kHz.[20]

Upon receiving an L1 Accept, the full raw data from all subdetectors are assembled by the event builder and distributed across a farm of hundreds of multi-core servers.[23] Here, the High-Level Trigger (HLT) runs near-online reconstruction algorithms—including track fitting, calorimeter clustering, and vertex reconstruction—to perform much more refined selection than is possible in hardware.[24, 25] These software algorithms reduce the data flow from the 30 kHz L1 rate to about 5 kHz of events that are ultimately recorded,[24, 25] ensuring that only the most promising physics candidates reach permanent storage while respecting bandwidth and computing limitations.

doi:10.6342/NTU202504255

Complementing these physics triggers are dedicated calibration and monitoring streams—laser calibration pulses, random triggers, and periodic triggers—that operate continuously alongside the main triggers.[26]

doi:10.6342/NTU202504255

Chapter 3

Particle Selection and Reconstruction

3.1 Sample

To refine the event selection and derive fitting models empirically, we employ both high-statistics signal-only samples and extensive generic Monte Carlo datasets. The generic MC is based on centrally produced, run-dependent BGx1 MC15rd samples, which include the processes $B^0\bar{B}^0$, B^+B^-, $u\bar{u}$, $d\bar{d}$, $c\bar{c}$, $s\bar{s}$, and $\tau^+\tau^-$, scaled to an integrated luminosity of $1.4ab^{-1}$ at the $\Upsilon(4S)$ resonance. For each signal decay channel, we simulate 1×10^6 events. Our analysis covers all LS1 $\Upsilon(4S)$ runs processed with the latest official proc13 calibration and alignment constants, including prompt reprocessing and data quality filtering:

- Exp 7 (proc13),
- Exp 8 (proc13),
- Exp 10 (proc13),
- Exp 12 (proc13),
- Exp 14 (proc13),

doi:10.6342/NTU202504255

- Exp 16 (proc13),
- Exp 17 (proc13),
- Exp 18 (proc13),
- Exp 20 (prompt),
- Exp 22 (prompt),
- Exp 24 (prompt),
- Exp 26 (prompt),

3.2 Reconstruction Modes

$B^+ \longrightarrow \omega(\pi^+\pi^-\pi^0)K^+$

$B^+ \longrightarrow \omega(\pi^+\pi^-\pi^0)\pi^+$

3.3 Reconstruction and preselection

The analysis employed the full basf2 package (release-light-2501-betelgeuse) for the channels $B^+ \to \omega(\pi^+\pi^-\pi^0)K^+$ and $B^+ \to \omega(\pi^+\pi^-\pi^0)\pi^+$. B-meson candidates were formed by first assembling collections of final-state particle candidates under loose baseline selection, and then subjecting these collections to kinematic fits tailored to the topology of each decay.

3.3.1 Charged Tracks Selection

For charged pions and kaons, we start from the all list and require $thetaInCDCAcceptance$, $nCDCHits > 20$, $dr < 0.5cm$, and $|dz| < 2cm$. Tracks with lisklihood ratio $\frac{\mathcal{L}_K}{\mathcal{L}_K+\mathcal{L}_\pi} > 0.6$ are identified as kaons. simultaneously, $\frac{\mathcal{L}_\pi}{\mathcal{L}_K+\mathcal{L}_\pi} > 0.6$ are identified as

doi:10.6342/NTU202504255

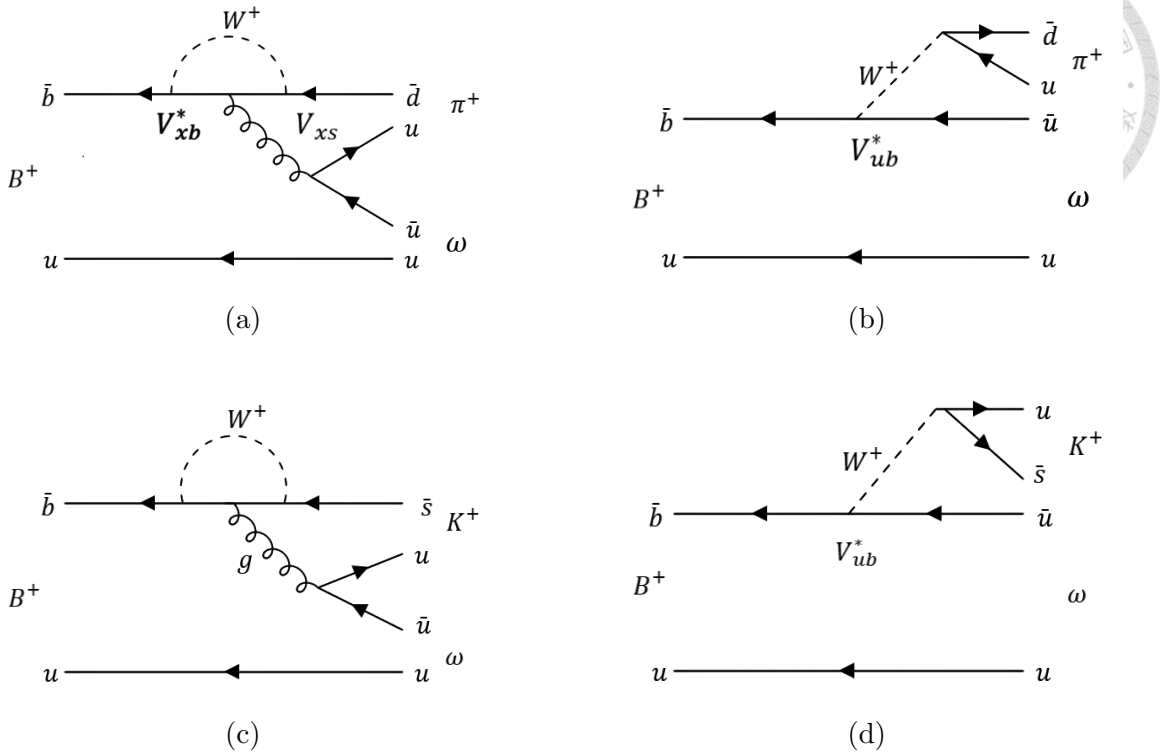

Figure 3.1: $B^+ \to \omega(\pi^+\pi^-\pi^0)K^+$ and $B^+ \to \omega(\pi^+\pi^-\pi^0)\pi^+$ Feynman diagrams.

pions.

3.3.2 gamma and π^0 selection

Candidate γ are reconstructed from clusters in the ECL not associated to a track using the gamma:pi0eff20_may2020 standard list. The standard list selects cluster within $0.2967 < \theta < 2.6180$ rad. The cluster are required to satisfy energy requirements depending on their spatial location $forward > 0.080GeV$, $barrel > 0.050GeV$ and $backward > 0.060GeV$.

Candidate π^0 are reconstructed by combining two γ candidates. After the reconstruction, the mass of the π^0 candidates is constrained to the nominal value by performing a mass constrained fit using kFit. We refrence the π^0 selection developed for $B^0 \to \pi^0\pi^0$. Streamlining it only by dropping the $abs(cosHelicityAngleMomentum)$.

doi:10.6342/NTU202504255

Especially, the official belle2 π^0 standard list require $-1.0 < daughterDiffOf(0,1,phi) < 1.0$ and $daughterAngle(0,1) < 0.9$ However, these cuts conflict with the variables we will use in our forthcoming fit, inducing a noticeable distortion in the background $\mathcal{H}_\omega$ shape. Consequently, we have chosen to remove both of these selection criteria.

3.3.3 ω reconstruction

The ω mesons are reconstructed in the $\pi^+\pi^-\pi^0$channel with the known branching fraction 89.1% (PDG) The $\pi^+\pi^-\pi^0$ combination suffers large background due to low energy γ and π^0 . From the inclusive ω data studies, the π^0 are required to have the list type eff20_may2020.

The ω candidates are required to have invariant mass within $\pm 30 MeV/c^2$window from the known ω mass of 782.57 MeV/c^2 . The natural width of ω is 8.44 MeV/c^2 , and the ω mass window cut within $\pm 30 MeV/c^2$ has more than 90% efficiency for a Breit-Wigner distribution.

3.3.4 B reconstruction

Reconstructed B meson candidates are selected using two nearly uncorrelated kinematic variables: the beam-energy-constrained mass $M_{bc} \equiv \sqrt{(E_{\rm beam}^{\rm CMS})^2 - (p_B^{\rm CMS})^2}$ and the energy difference $\Delta E \equiv E_B^{\rm CMS} - E_{\rm beam}^{\rm CMS}$. Here, $E_{\rm beam}^{\rm CMS}$ is the beam energy and $E_B^{\rm CMS}$, $p_B^{\rm CMS}$ are the reconstructed energy and momentum of the B candidate in the e^+e^- center-of-mass system. The M_{bc} distribution exhibits a sharp peak at the nominal B mass with a typical resolution of $\mathcal{O}(3\,{\rm MeV}/c^2)$, providing strong separation from lower-mass backgrounds, while ΔE peaks at zero for correctly reconstructed signals and shifts for misreconstructed or partially lost events, offering powerful discrimination against combinatorial and continuum backgrounds. We initially retain candidates with loose requirements $M_{bc} > 5.2\,{\rm GeV}/c^2$ and $|\Delta E| < 0.25\,{\rm GeV}$ to maintain high signal efficiency for subsequent multivariate continuum suppres-

doi:10.6342/NTU202504255

sion and maximum-likelihood fitting. Final selection windows are then optimized to maximize signal significance and purity.

3.4 Summary of Event Selection

In this section,we listed the Event selection for the two decay modes.

Final state particle selection	
K^+	BinaryKπID > 0.6 thetaInCDCAcceptance dr < 0.5 cm abs(dz) < 2 cm nCDCHits > 20
π^+	BinaryKπID < 0.4 thetaInCDCAcceptance dr < 0.5 cm abs(dz) < 2 cm nCDCHits > 5
γ	clusterE > 0.025 GeV thetaInCDCAcceptance clusterNHits > 1.5 $0.2967 <$ clusterTheta < 2.6180 clusterReg=1 for E >0.080 GeV clusterReg=2 for E >0.050 GeV clusterReg=3 for E >0.060 GeV clusterE1E9 <0.9
Reconstructed particle selection	
π^0	abs($\cos\theta_{hel}$) <0.97 $0.121 < M_{\gamma\gamma} < 0.142$ GeV
ω	812.57 MeV $>$ InvM $>$ 752.57 MeV
B^+	Mbc >5.2 abs(ΔE) <0.25

Table 3.1: Selection criteria for the ωK^+ channel.

Final state particle selection	
π^+	BinaryKπID < 0.4 thetaInCDCAcceptance dr < 0.5 cm abs(dz) < 2 cm nCDCHits > 5
γ	clusterE > 0.025 GeV thetaInCDCAcceptance clusterNHits > 1.5 $0.2967 <$ clusterTheta < 2.6180 clusterReg=1 for E >0.080 GeV clusterReg=2 for E >0.050 GeV clusterReg=3 for E >0.060 GeV clusterE1E9 <0.9
Reconstructed particle selection	
π^0	abs($\cos\theta_{hel}$) <0.97 $0.121 < M_{\gamma\gamma} < 0.142$ GeV
ω	812.57 MeV $>$ InvM $>$ 752.57 MeV
B^+	Mbc >5.2 abs(ΔE) <0.25

Table 3.2: Selection criteria for the $\omega\pi^+$ channel.

doi:10.6342/NTU202504255

Chapter 4

Background

In charmless B decay studies, background contributions can be broadly classified into two categories: combinatorial background and $B\overline{B}$ background.

The dominant background arises from combinatorial background, which originates from the continuum processes: $e^+e^- \longrightarrow q\overline{q}$ processes. In these events, hadrons produced from quark-antiquark fragmentation are randomly combined to form fake B candidates, leading to a smooth distribution in kinematic variables such as M_{bc}andΔE.

The other is $B\overline{B}$ background,which comes form $\Upsilon(4S) \longrightarrow B\overline{B}$ including :

• Mis-reconstructed events, where incorrect particle assignments lead to an event being misidentified as a charmless B decay.

• Feed-across background, in which a decay mode with similar final-state particles but different intermediate states contributes to the reconstructed sample.

• Rare B decays, such as $B \longrightarrow DX$, where a charm decay is mistakenly classified as a charmless decay due to missing or misidentified particles.

4.1 Combinatorial Background

In the Belle II experiment at an e^+e^- collider, the $\Upsilon(4S)$ resonance decays almost exclusively to a pair of spin-0 $B\overline{B}$ mesons. Because the parent $\Upsilon(4S)$ has spin 1,

doi:10.6342/NTU202504255

the angular distribution of its decay follows

$$\frac{\mathrm{d}\Gamma}{\mathrm{d}\cos\theta_B} \propto \sin^2\theta_B$$

where θ_B is the angle between the B meson and the beam axis. In contrast, continuum light-quark pairs ($q\overline{q}$) from $e^+e^- \to q\overline{q}$ behave like spin-$\frac{1}{2}$ fermions and exhibit

$$\frac{\mathrm{d}\sigma}{\mathrm{d}\cos\theta_B} \propto 1 + \cos^2\theta_B$$

This marked difference in topology underpins our "continuum suppression" strategy.

To exploit these shape differences, we train a binary boosted decision tree (FBDT) within the basf2 framework to separate $B\overline{B}$ signal from continuum $q\overline{q}$ background. The FBDT uses 41 carefully chosen input variables that are largely uncorrelated with the key kinematic observables M_{bc} and ΔE. These inputs include:

- Flavor-tagger outputs and vertex-fit quality metrics,
- Thrust and modified Fox–Wolfram moments,
- Event sphericity and other global shape descriptors,
- Kinematic-fit chi-square and track-quality indicators,
- And several additional non-linear combinations of reconstructed quantities.

A full description of each variable and its physical motivation is given in the following sections.

4.1.1 Thrust Angle

The thrust axis $\overrightarrow{T}$ is defined as the unit vector $\overrightarrow{T}$ which maximizes the projection of all particle momenta onto itself, and the thrust magnitude is

$$T = \frac{\sum_{i=1}^{N} \left| \overrightarrow{p_i} \cdot \overrightarrow{T} \right|}{\sum_{i=1}^{N} \left| \overrightarrow{p_i} \right|} . \tag{4.1}$$

doi:10.6342/NTU202504255

The thrust angle $\theta_{\rm thr}$ is then defined as the angle between the thrust axis of the B candidate, $\overrightarrow{T}_B$, and the thrust axis of the rest of the event (ROE), $\overrightarrow{T}_{\rm ROE}$:

$$\cos\theta_{\rm thr} \;=\; \overrightarrow{T}_B \;\cdot\; \overrightarrow{T}_{\rm ROE}\,.$$

In continuum $q\overline{q}$ events, which form two nearly back-to-back jets, the two thrust axes tend to align, so $|\cos\theta_{\rm thr}|$ peaks near 1. By contrast, in true $B\overline{B}$ events the decay products are more isotropic and the distribution of $\cos\theta_{\rm thr}$ is much flatter. Therefore, including $|\cos\theta_{\rm thr}|$ as an input to the boosted decision tree provides strong discrimination between signal and continuum background.

One can also define the thrust angle relative to the beam axis,

$$\cos\theta_B^{\rm thrust} \;=\; \hat{z} \;\cdot\; \overrightarrow{T}_B\,,$$

which follows a $\sin^2\theta_B^{\rm thrust}$ distribution for signal and a $1+\cos^2\theta_B^{\rm thrust}$ distribution for continuum, further enhancing separation when used in combination with other shape variables.

4.1.2 Flavor Tagging

Flavour tagger gives the flavour of the tagged B meson, and the information from the tage-side B decay[27].The following flavour taggeing variables are we used to seperate the signal and backgrounds.

- *qpKinLepton* :charge of the tag-side track with highest probability of being a primary lepton multiplied by the respective probability.
- *qpKaon*:charge of the tag-side track with highest probability of being a $b \to c \to s$ kaon multiplied by the respective probablity
- *qpSlowPion*:charge of the tag-side track with highest probability of being a

doi:10.6342/NTU202504255

slow pion from the decay of a primary D^* multiplied by the respective probability.

- FBDT-qrCombined:combined flavor q times dilution factor r.

4.1.3 Vertex

Compare to other light meson, the life time of B meson is longer. Because of the boost between $\Upsilon(4S)$ and laboratory systems, B meson typically has longer flight distance Because real $B\bar{B}$ events have a displaced decay vertex while continuum light-quark pairs do not, we use a few simple vertex observables:

- **Flight-distance significance:** $\frac{L}{\sigma_L}$, larger for B decays.
- Δz**:** the distance along the beam axis between the two B-vertex z positions.
- **Vertex fit quality:** $\chi^2_{\rm vtx}$, smaller for well-defined secondary vertices.

4.1.4 Fox-Wolfram moments

For a collection of N particles with momenta p_i,the l^{th} order Fox-Wolfram moment H_l is defined as

$$H_l = \sum_N^{i,j} |p_i|\,|p_j|\,P_l(cos\theta_{i,j}) \tag{4.2}$$

The original Fox–Wolfram moments are defined by

$$H_l \;=\; \sum_{i,j} |p_i|\,|p_j|\,P_l\big(\cos\theta_{ij}\big)\,, \tag{4.3}$$

where θ_{ij} is the angle between particles i and j in the center-of-mass frame, and P_l is the lth-order Legendre polynomial. To improve discrimination between spherical $B\bar{B}$ events and jet-like continuum ($e^+e^- \to q\bar{q}$), Belle introduced the *modified* moments, in which one separates the sums over the signal B-candidate daughters

doi:10.6342/NTU202504255

(s) and the rest-of-event (o), and applies momentum weights w_k (typically $|\vec{p}_k|$ or energy in the CM frame). The general form is

$$H_l^{XY} \;=\; \sum_{i\in X}\sum_{j\in Y} \frac{w_i\, w_j}{\left(\sum_k w_k\right)^2}\, P_l\big(\cos\theta_{ij}\big), \quad X, Y \in \{s, o\}, \tag{4.4}$$

with the normalization chosen so that $H_0^{XX} = 1$. In particular one computes three basic types:

$$H_l^{ss} = \sum_{i,j\in s} \frac{w_i w_j}{(\sum_k w_k)^2}\, P_l(\cos\theta_{ij}), \tag{4.5}$$

$$H_l^{so} = \sum_{i\in s}\sum_{j\in o} \frac{w_i w_j}{(\sum_k w_k)^2}\, P_l(\cos\theta_{ij}), \tag{4.6}$$

$$H_l^{oo} = \sum_{i,j\in o} \frac{w_i w_j}{(\sum_k w_k)^2}\, P_l(\cos\theta_{ij}). \tag{4.7}$$

To further exploit particle-type information from the rest-of-event, the *so* term is split into three sub-components,

$$H_{xl}^{so} = \sum_{i\in s}\sum_{j\in o_x} \frac{w_i\, w_j}{(\sum_k w_k)^2}\, P_l\big(\cos\theta_{ij}\big), \quad x \in \{c, n, m\}, \tag{4.8}$$

where "c" denotes charged particles, "n" neutrals, and "m" missing (e.g. tracks below threshold). Finally one defines the normalized ratios

$$R_l^{XY} \;=\; \frac{H_l^{XY}}{H_0^{mod}}, \quad R_{xl}^{so} \;=\; \frac{H_{xl}^{so}}{H_0^{mod}}, \tag{4.9}$$

with $H_0^{mod} = 1$ by construction. Of these, R_2 (and especially $R_{2\,cl}^{so}$) provide the strongest separation between $B\bar{B}$ and continuum, and are hence widely used both in skimming and in final event selection. To characterize event shapes, we use the original Fox–Wolfram definition of H_l[28] and adopt the Belle experiment's improved scheme of separating the signal and rest-of-event contributions with momentum weighting [29][30].

doi:10.6342/NTU202504255

4.1.5 CLEO Cone

In particle physics, a "cone" refers to a conical region centered around a given direction within a fixed angular range. The CLEO Cone variable typically uses the motion direction of a candidate particle (such as a B meson) as the reference axis, dividing the other particles into several fixed angular intervals based on their angle relative to this axis (for example $0° - 10°$, $10° - 20°$, $20° - 30°$,etc),and there are nine concentric cones totally. For each conical region, the total energy or momentum of all particles within the region is calculated, forming a set of numerical values that describe the event's energy distribution. These values reflect the flow and distribution of energy within the event. In this study, we only use the Cleo Cones variables calculated from $ROE(CleoConeCS(i, ROE))$ to reduce the correlation with M_{bc} and ΔE.

4.1.6 Training Consequence and F.O.M

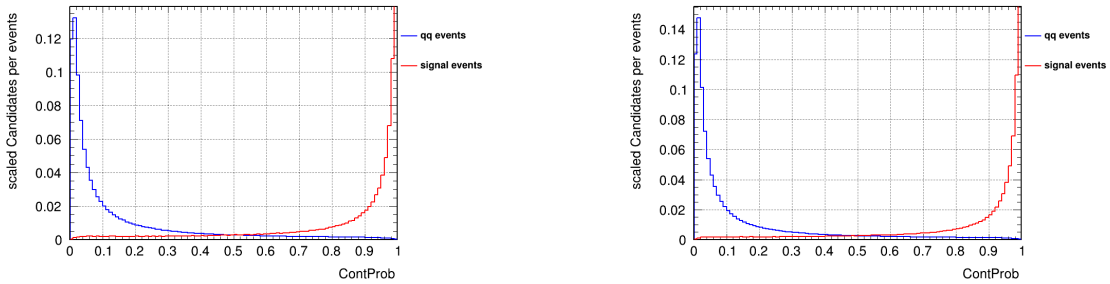

Figure 4.1: Distribution of FastBDT Output,left side is ωK^+mode right side is $\omega\pi^+$mode

To optimize background suppression, we scan the FastBDT score threshold and choose the cut that maximizes the figure of merit (F.O.M.), defined as

$$F.O.M = \frac{S}{\sqrt{S+B}} \tag{4.10}$$

Where S and B is the number of signal and background events in signal region(the signal region is choosen as $M_{bc} > 5.27GeV$ and $-0.15GeV < \Delta E < 0.1GeV$)

doi:10.6342/NTU202504255

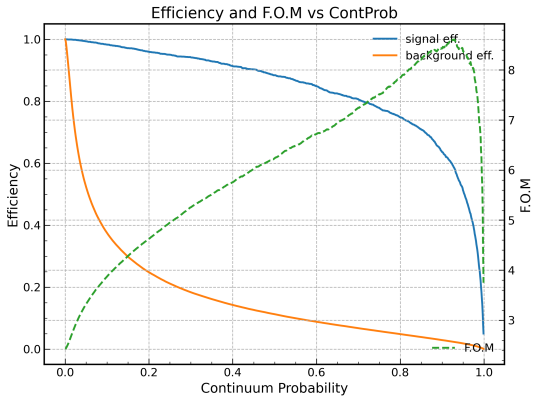

(a) K mode

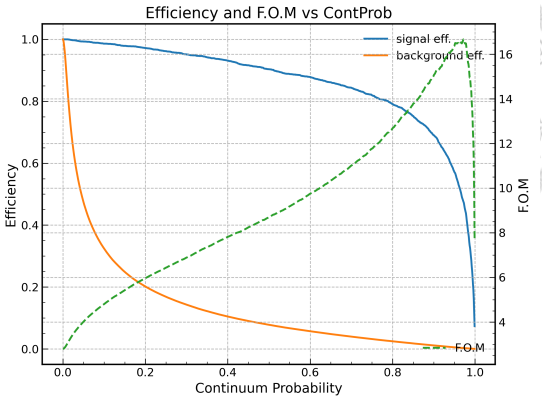

(b) π mode

Figure 4.2: The figure of merit for $B^+ \to \omega h^+$ modes

4.2 $B\overline{B}$ Background

Generic $B\bar{B}$ background originates from all B decay modes except the signal channel $B^+ \to \omega(\pi^+\pi^-\pi^0)\, h^+$.Unlike continuum $q\bar{q}$ background, these contributions are not combinatorial but stem from misreconstructed B decays that peak in our fit region and are therefore challenging to model. To study them, we reconstruct candidates in a generic $B\bar{B}$ Monte Carlo sample by selecting decay modes according to the Belle II decay table, then validate each by matching the reconstructed decay chain against MC truth information and the decay-hash table.

4.3 Feed-Across Background

Feed-across background originates from signal-like decays in which the bachelor kaon and pion are misidentified.Because the kinematics are almost identical, these events populate the same region of the beam-constrained mass M_{bc} and energy difference ΔE, but with a shifted ΔE peak due to the wrong mass hypothesis:

$$\Delta E = E_B - E_{\mathrm{beam}},$$

doi:10.6342/NTU202504255

where E_B is computed assuming the incorrect mass for the bachelor track. The resulting ΔE distribution appears signal-like in shape (narrow and peaking), but its mean is displaced by

$$\delta(\Delta E) \sim \pm(m_K - m_\pi)\,\frac{p}{E}\,,$$

making it distinguishable from true signal. In our fits, we therefore include a separate "feed-across" PDF component—often modeled with a shifted Gaussian or Crystal Ball function—to account for this peaking background and avoid biasing the signal yield or CP-asymmetry measurement.

4.4 Self Cross-Feed

In charmless hadronic B-meson decay analyses, self–cross–feed (SCF) refers to events that truly originate from a signal decay (e.g. $B \to h_1 h_2$) but are misreconstructed—for example, a companion-B pion is swapped into the signal candidate, a π^0 photon pair is paired incorrectly (or one photon is missed/duplicated), or electrons/photons are misidentified—yet still pass the signal selection. These SCF events typically populate the region around the signal peaks in kinematic variables such as $M_{\rm bc}$ and ΔE, but leave distortions in the tails or shifts in the energy distribution. To prevent this "self-contamination" from being counted as true signal, we first tags and quantifies SCF in Monte Carlo using truth-level information—measuring its fraction and shapes in each observable—then includes SCF. Then we would check the ratio of the SCF to decide if we need set it as a separate component in the final signal + background fit.

4.5 Best Candidate

After all selection requirements are imposed, there are still some events have multiple candidates. The B candidate multiplicity of is about 1.108, and is about 1.106

doi:10.6342/NTU202504255

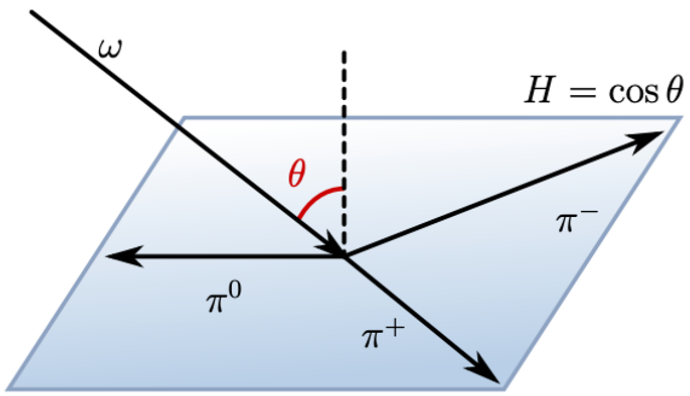

Figure 4.3: The defination of the ω Helicity

In this study we choose the χ^2 probability to restrict the number of candidates per events.

4.6 Summary for Final Selection

In table 4.1 and 4.2 we summary the corsponding efficiency after different selection. And The final distribution of Three fitting component have been showed in **??** and **??**.

We have we construct the helicity variable $\mathcal{H}_\omega$ of the ω candidates, defined as the cosine of the angle between the flight direction of the ω candidate and the normal to the plane of the three pions it decays to. The theoretical distribution of the variable in real ω meson is a symmetry quartic formula.

Table 4.1: Signal selection efficiencies at each analysis stage.

Selection stage	**Signal efficiency**
Preselection and reconstruction	41.70%
M_{bc} & ΔE	40.89%
PID	35.70%
π^0 veto	30.50%
ω mass window cut	23.17%
CSMVA cut	13.90%
Best candidate	13.40%

doi:10.6342/NTU202504255

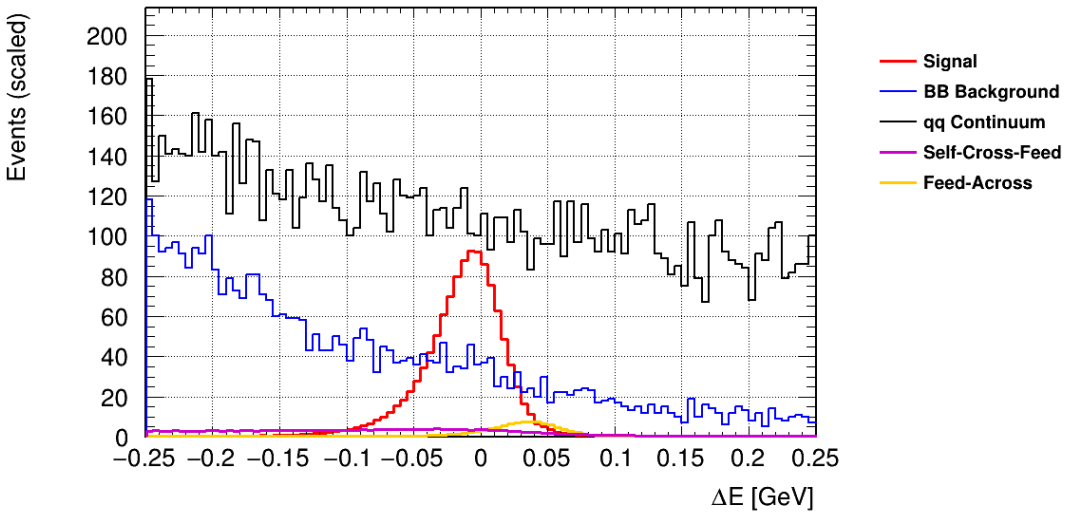

Figure 4.4: ΔE for $\omega K^{\pm}$

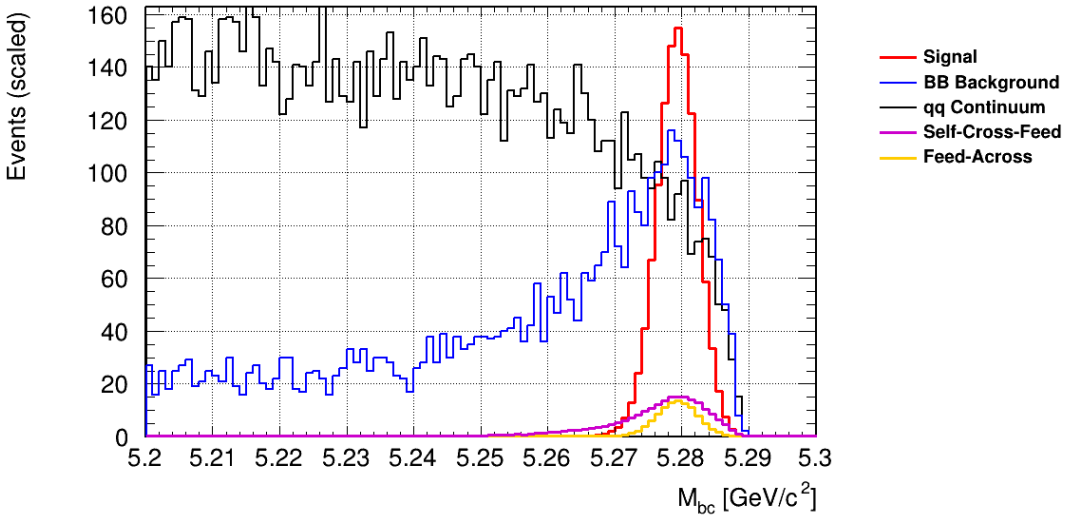

Figure 4.5: $M_{\rm bc}$ for $\omega K^{\pm}$

Table 4.2: Signal selection efficiencies at each analysis stage.

Selection stage	**Signal efficiency**
Preselection and reconstruction	44.5 %
M_{bc} & ΔE	44.2 %
PID	37.7 %
π^0 veto	32.5 %
ω mass window cut	25.27%
CSMVA cut	15.1 %
Best candidate	14.62%

doi:10.6342/NTU202504255

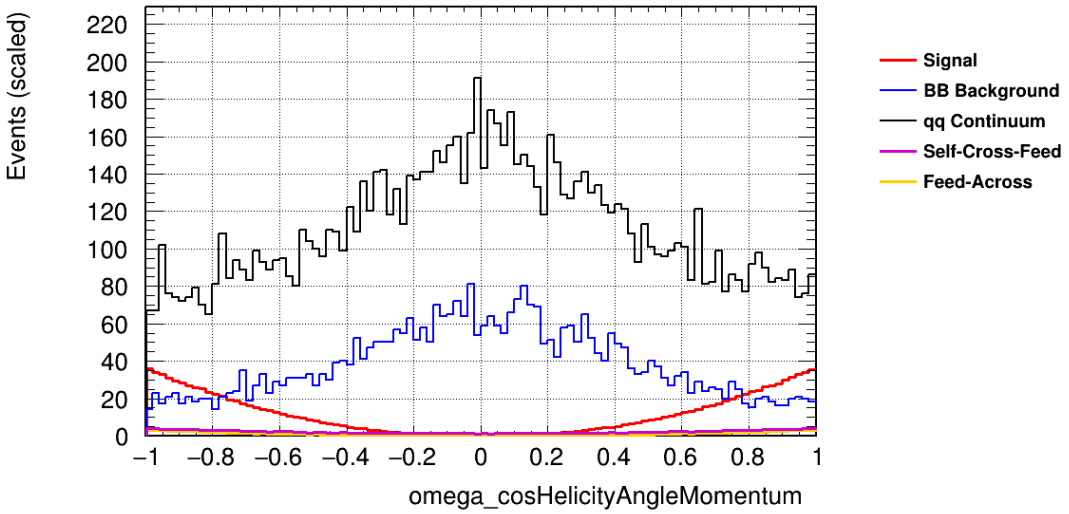

Figure 4.6: $\mathcal{H}_\omega$ for $\omega K^\pm$

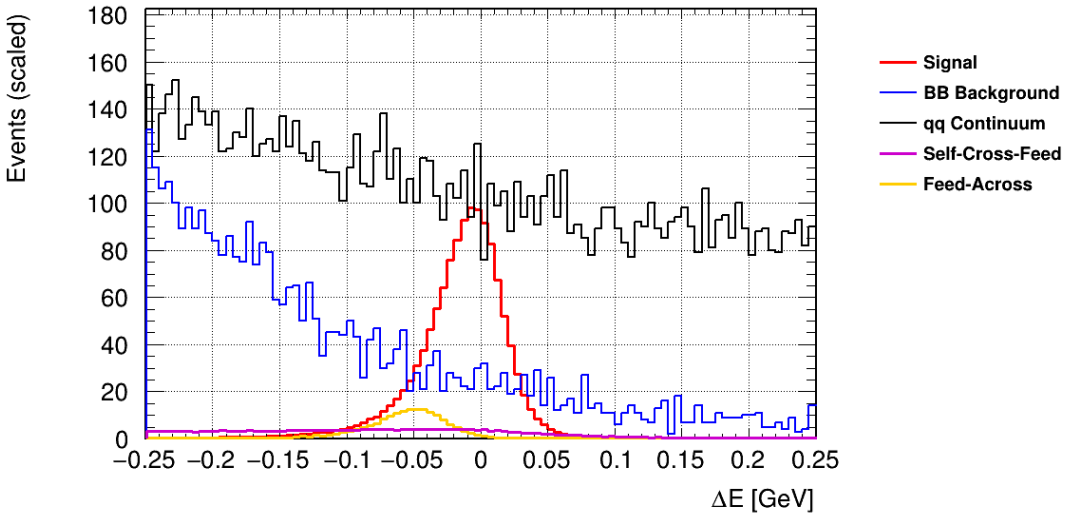

Figure 4.7: ΔE for $\omega\pi^\pm$

doi:10.6342/NTU202504255

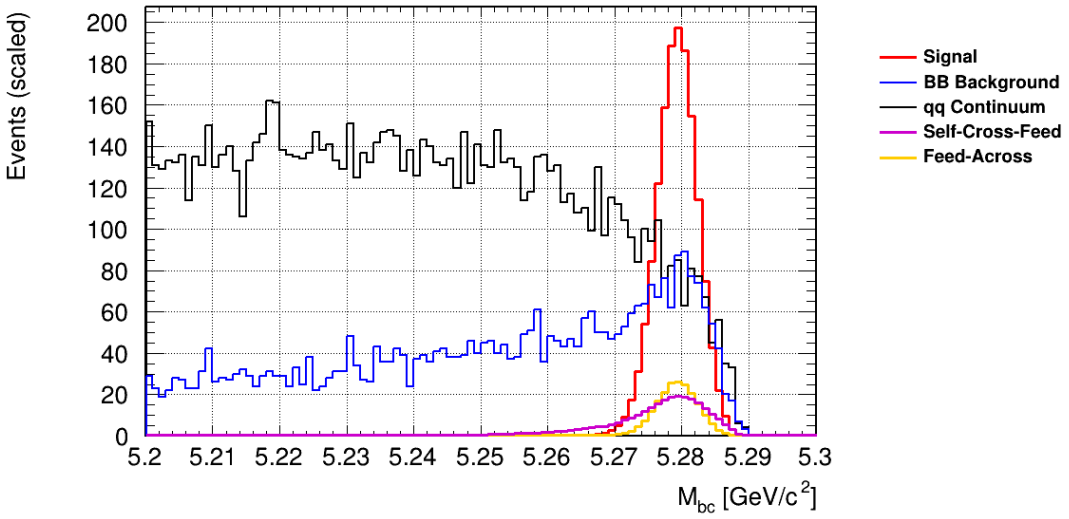

Figure 4.8: $M_{\rm bc}$ for $\omega\pi^{\pm}$

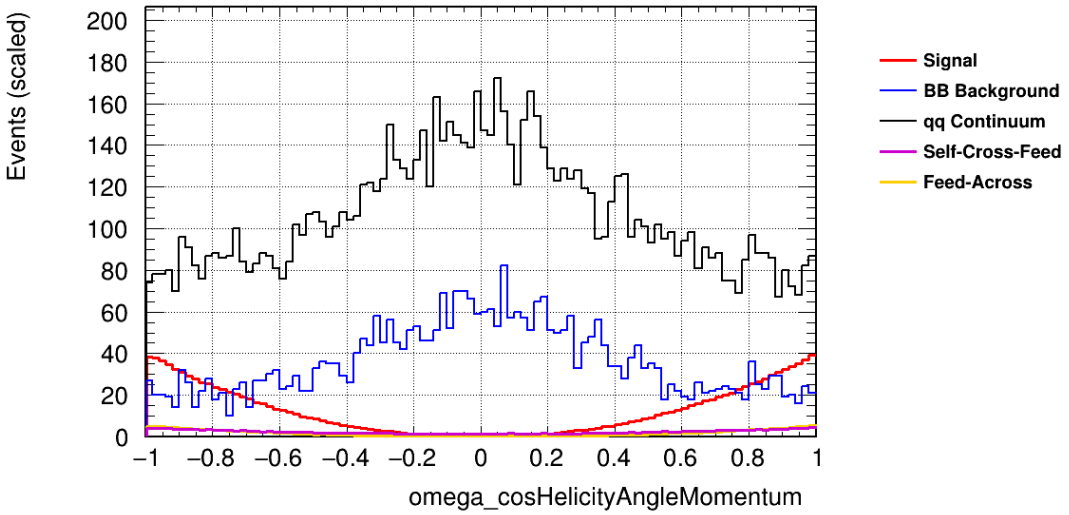

Figure 4.9: $\mathcal{H}_{\omega}$for $\omega\pi^{\pm}$

doi:10.6342/NTU202504255

Chapter 5

Signal Extraction

It is planed to use 3-dimensional un-binned ML fit including the M_{bc} ΔE and $\mathcal{H}_\omega$, to get the number of signal yields

For the simultaneous fit of the samples, It is considered using 4 components per sample: Signal, $B\bar{B}$ background, $q\bar{q}$ background and feed-acorss Background.

For the self-cross-feed background, Because of ralitively low ratio compare to signal events $\frac{S}{S+B} = 5.87\%$) in the signal region($M_{bc} > 5.27$ and $-0.15 < \Delta E < 0.1$), for whole region the ratio is $5.8\%(\omega K^+)$ and $4.8\%(\omega\pi^+)$ It was not set as a single component

5.1 Correlation Check

Photon energy leakage in rare charmless B decays introduces a long low-energy tail in the ΔE distribution and produces a strong correlation between ΔE and M_{bc}. Since this correlation invalidates modeling ΔE, M_{bc}, and the third variable independently, we first evaluate their interdependence before constructing separate PDFs. The details are put in the Appenidx.5.

doi:10.6342/NTU202504255

Table 5.1: Correlation coefficients between fit variables for different components in the ωK^+ decay channel.

Component	Mbc–ΔE	Mbc–$\mathcal{H}_\omega$	ΔE–$\mathcal{H}_\omega$
$q\bar{q}$	1.06	– 0.33	– 1.60
$B\bar{B}$	– 2.48	0.53	1.28
signal	– 5.90	0.04	0.000 31
feed-across	– 0.90	0.022	0.16

Table 5.2: Correlation coefficients between fit variables for different components in the $\omega\pi^+$ decay channel.

Component	Mbc–ΔE	Mbc–$\mathcal{H}_\omega$	ΔE–$\mathcal{H}_\omega$
$q\bar{q}$	1.17	– 0.24	– 1.60
$B\bar{B}$	– 3.57	0.45	1.28
signal	−0.043	−0.0015	−0.000 36
feed-across	– 0.98	0.031	0.18

5.2 PDF Modeling

the used PDFs are summarized in Table 6.2 and we put the modeling details in **??**

5.2.1 Signal Model

The PDF for ΔE is sum of one Bifurcated Gaussian and one Crystal Ball function. The PDF for M_{bc} is sum of one Bifurcated Gaussian and one Gaussian. The $\mathcal{H}_\omega$ shape is modeled with the sum of symmetric Chebyshev polynomials up to 4th order. We use the region $-0.15GeV \leq \Delta E \leq 0.1GeV$ and $5.26GeV \leq \Delta E \leq 5.288GeV$ as our model region the decide our fitter and reject the large fluctuation of the events in the tail. Nevertheless, the model is precise enough because less than 1% of the signal events are in the tails.

5.2.2 Feed-across Model

Feed-across events has similar distribution with signal events but has different peak in ΔE which can help us to seperate it with signal events. We use similar strategy

doi:10.6342/NTU202504255

to model the Feed-across events.

5.2.3 $q\bar{q}$ Model

The Continuum Back ground comes form combinatorial backgournds.So there is no either peak in our fitting region or have strong correlation. An argus funciton is used to model the M_{bc} and a first order polynomial is used to model the ΔE. The $\mathcal{H}_\omega$ shape is modeled with the sum of a 1^{st} Polynomial and a Gaussian.

5.2.4 $B\bar{B}$ Model

Charmless B meson background distributions are determined from a large MC sample containing both $b \to c$ and $b \to u, d, s$ transitions. The ΔE distribution is modeled by a first-order Chebyshev polynomial $P_1(\Delta E)$ to describe the smooth combinatorial background, together with a Gaussian function $G(\Delta E; \mu_{\Delta E}, \sigma_{\Delta E})$ whose mean $\mu_{\Delta E}$ is placed near $-0.25\,\mathrm{GeV}$ to account for partially reconstructed or misidentified decays. The beam-energy-constrained mass $M_{bc} \equiv \sqrt{(E_{\mathrm{beam}}^{\mathrm{CMS}})^2 - (p_B^{\mathrm{CMS}})^2}$ shape combines an ARGUS function $\mathcal{A}(M_{bc}; \xi, M_{\max}) \propto M_{bc}\sqrt{1-(M_{bc}/M_{\max})^2}\exp[\xi(1-(M_{bc}/M_{\max})^2)]$ with $M_{\max}$ fixed to the beam energy, and an asymmetric Gaussian $G_{\mathrm{asym}}(M_{bc}; \mu_{M_{bc}}, \sigma_L, \sigma_R)$ to model non-Gaussian tails from detector resolution. Finally, the ω helicity angle distribution $\mathcal{H}_\omega \equiv \cos\theta_\omega$ is described by the sum of a first-order polynomial in $\mathcal{H}_\omega$ and a Gaussian centered at the signal-like peak of the $\omega \to \pi^+\pi^-\pi^0$ decay. All shape parameters are extracted from MC fits and validated on data control regions before being used in the final signal extraction.

The ωK^+ and $\omega\pi^+$ mode has similar distribution so we use same Modeling ways. The modeling details are listed below.

doi:10.6342/NTU202504255

Table 5.3: Model functions used for different components in each variable.

Component	**Mbc**	ΔE	$\mathcal{H}_\omega$
Continuum background	Argus	First-order polynomial	Gaussian + 1^{st} polynomial
Generic background	Argus + Asymmetric Gaussian	Gaussian + 1^{st} polynomial	Gaussian + 1^{st} polynomial
Signal	Gaussian + bifurcated Gaussian	Bifurcated Gaussian + Crystal Ball functions	4^{th} symmetric Chebyshev
Feed across	Gaussian + bifurcated Gaussian	2 Crystal Ball functions	2^{nd} polynomial

5.3 Fitter Detials

Table 6.2 summrized the PDF modeling function. We use same funtion for the Two decay modes, and the PDF modeling details have been put in the Appendix.2. About fitting the $B^+ \longrightarrow \omega(\pi^+\pi^-\pi^0)K^+$ and $B^+ \longrightarrow \omega(\pi^+\pi^-\pi^0)\pi^+$ signal and feed-across yields, we fit directly for their branching ratios and direct CP asymmetry. Here we do not use the simutaneous fit for both two modes but regard them as two independent fitting:

$$N^{\pm} = N_{B^+B^-} * \mathcal{B} * \epsilon * \frac{1 \mp A_{cp}}{2} \tag{5.1}$$

5.4 Fitter Test

In this study, we validate the fitter bias by performing a toy test and ensemble test. The toy test use the PDF-generated data as a data sample for each component; the ensemble test uses MC samples from each component as simulated a data sample.Then we would use the pull distribution to test if our test would have bias.

$$Pull = \frac{x_{fit} - x_{input}}{\sigma_x} \tag{5.2}$$

doi:10.6342/NTU202504255

The details will be discussed in the following subsection and the results of fitter test will also be shown in this section.

5.4.1 Toy Test

Toy tests are a fast validation technique based purely on constructed probability model (PDF). We generate a large number of pseudo-data sets at the theoretical level via Monte Carlo sampling, then fit each one and examine both the average bias of the fitted parameters and the mean and width of the pull distribution.

5.4.2 Ensemble Test

In our GSIM ensemble tests, the "data" are generated from fully simulated Monte Carlo samples that pass through the full GEANT-based detector simulation and reconstruction. The signal and feed-across components come from pure signal MC, while the $B\bar{B}$ and $q\bar{q}$ backgrounds use the official generic MC samples. Unlike toy tests, which draw events from analytical PDFs, these ensemble tests include realistic detector effects, selection efficiencies, and variable correlations. As a result, any mismodeling or residual correlations in our PDFs will affect the fitted results. By fitting many such simulated datasets, we can better estimate statistical fluctuations, fit biases, and systematic effects, closely mimicking real data behavior. However, GSIM tests place stringent requirements on the sample size, as no event should be reused across pseudo-experiments. Currently, the Belle II collaboration provides only $1.4ab^{-1}$ worth of MC events, which—after applying our selection criteria—are far too few for conducting a large number of ensemble tests. Reusing events would introduce significant biases in the fit results. To avoid this issue, we replace the $B\bar{B}$ and $q\bar{q}$ background events with toy-generated samples in our ensemble study.

doi:10.6342/NTU202504255

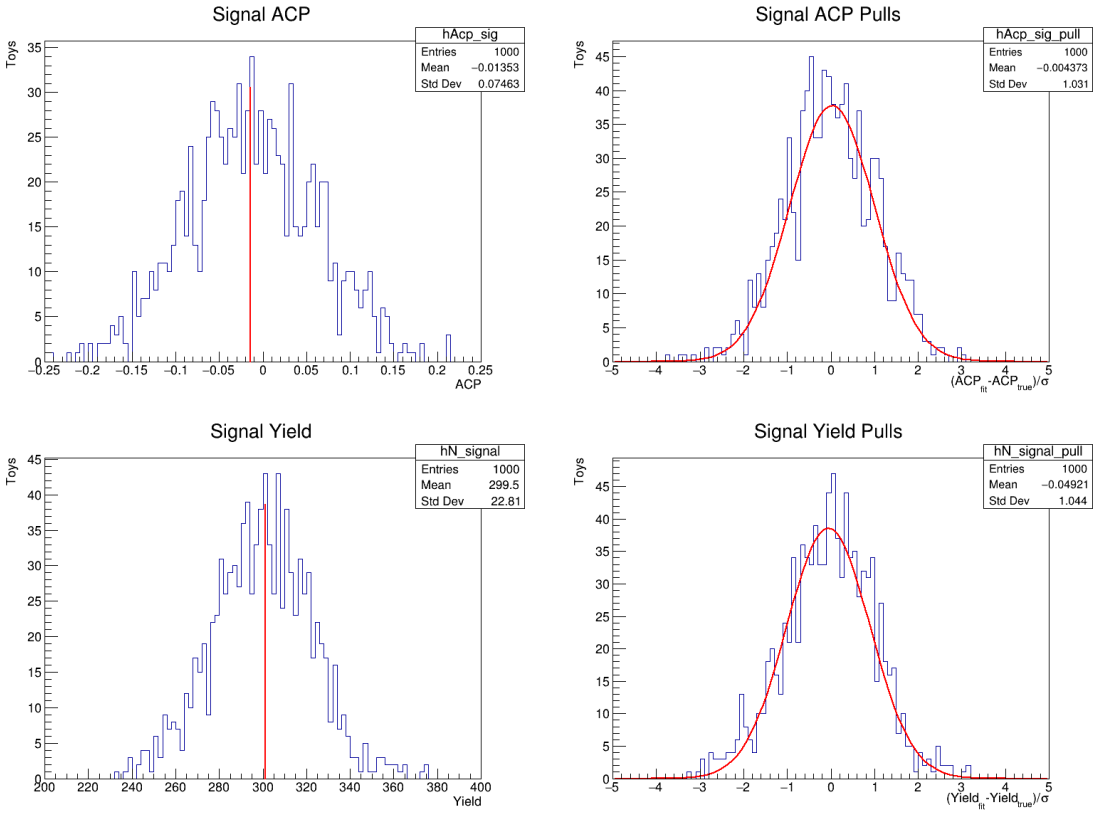

Figure 5.1: ωK^+ gsim test result

Table 5.4: The Gsim Test Result of $\omega\pi^+$

Input Value	Fitting value	Fitting error	Mean of pull	Width of pull
0.000 790	−0.006 252	−0.005 462	−0.030	0.9698
372.9	372.2	−0.7	−0.0515	0.9709

Table 5.5: The Gsim Test Result of ωK^+

Input Value	Fitting value	Fitting error	Mean of pull	Width of pull
−0.013 922	−0.014 079	−0.000 157	0.0356	0.9828
301.2	299.5	−1.7	−0.0515	0.9774

doi:10.6342/NTU202504255

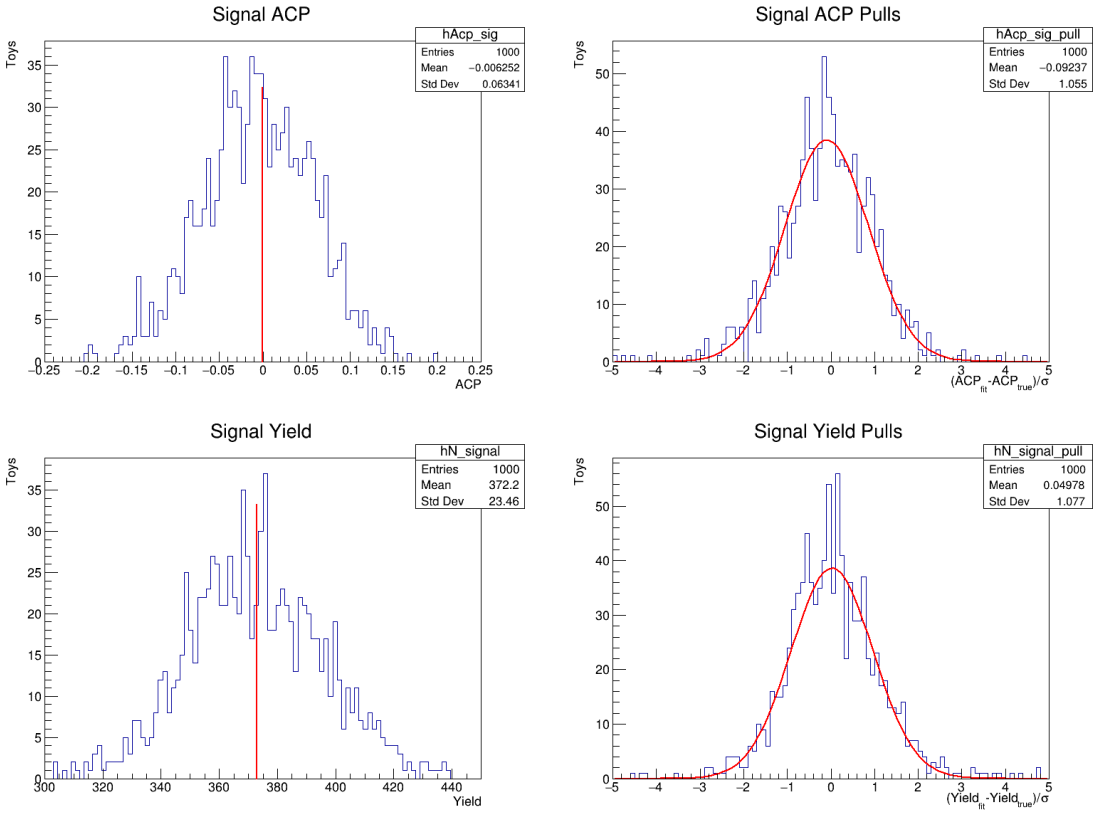

Figure 5.2: $\omega\pi^+$ gsim test result

doi:10.6342/NTU202504255

5.5 Linearity Check

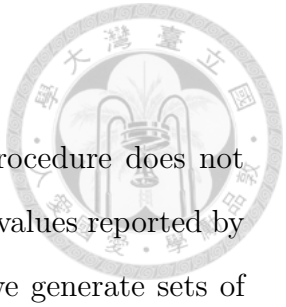

Additionally, we perform linearity tests to verify that our fit procedure does not introduce any bias when the true A_{CP} deviates from the nominal values reported by the PDG. For each decay mode ($B^+ \to \omega K^+$ and $B^+ \to \omega \pi^+$), we generate sets of ToyMC pseudo-experiments with the input asymmetry, $A_{\mathrm{CP}}^{\mathrm{true}}$, varying in steps from -1.0 to $+1.0$. At each input value we produce 500 independent pseudo-datasets, each containing the same total yield as in the nominal fit, and then fit each dataset with our full 3-dimensional model, allowing only the CP asymmetry parameter to float.

We define the average fitted asymmetry,

$$\langle A_{\mathrm{CP}}^{\mathrm{fit}} \rangle = \frac{1}{N_{\mathrm{toys}}} \sum_{i=1}^{N_{\mathrm{toys}}} A_{\mathrm{CP},\,i}^{\mathrm{fit}} \,,$$

and the bias,

$$\Delta A_{\mathrm{CP}} = \langle A_{\mathrm{CP}}^{\mathrm{fit}} \rangle - A_{\mathrm{CP}}^{\mathrm{true}} \,. \tag{5.3}$$

A perfectly linear response would yield $\Delta A_{\mathrm{CP}} = 0$ for all inputs, and the slope of a linear fit of $\langle A_{\mathrm{CP}}^{\mathrm{fit}} \rangle$ versus $A_{\mathrm{CP}}^{\mathrm{true}}$ should be unity.

For each mode we then fit the points $\left(A_{\mathrm{CP}}^{\mathrm{true}},\, \langle A_{\mathrm{CP}}^{\mathrm{fit}} \rangle\right)$ to

$$\langle A_{\mathrm{CP}}^{\mathrm{fit}} \rangle = p_0 + p_1 \, A_{\mathrm{CP}}^{\mathrm{true}} \,,$$

extracting the intercept p_0 and slope p_1. Deviations of p_0 from zero or p_1 from one indicate residual fit bias or non-linearity.

The results of the linearity tests are shown in Fig. 6.1. In both decay channels, the fitted slopes are consistent with unity within statistical uncertainties, and the intercepts are consistent with zero, demonstrating that our CP asymmetry extraction is unbiased over the full physical range.

doi:10.6342/NTU202504255

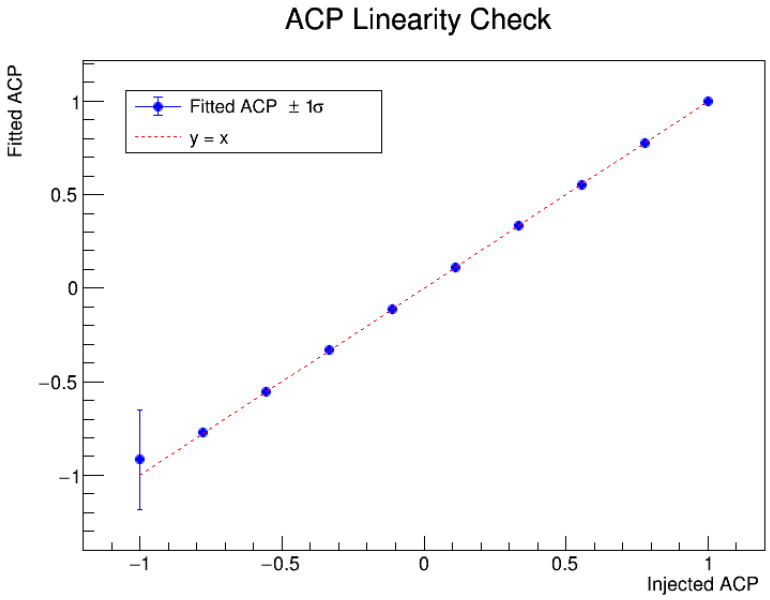

Figure 5.3: linearity check for CP asymmetry in ωK^+

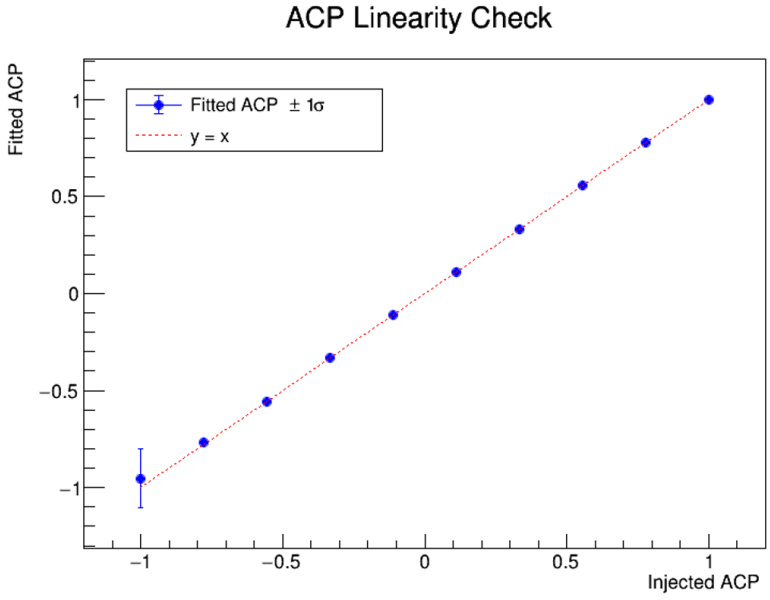

Figure 5.4: linearity check for CP asymmetry in $\omega\pi^+$

doi:10.6342/NTU202504255

Chapter 6

Control Sample

To assess discrepancies between data and Monte Carlo simulation, we employ a high-statistics control channel with well-known kinematics to derive data-driven corrections for selection efficiencies and background models.

We use the decay

$$B^+ \to \bar{D}^0\pi^+, \quad \bar{D}^0 \to K^+\pi^-\pi^0,$$

which benefits from a large branching fraction and shares the same final state as our signal, providing abundant events and precise PDG inputs.

6.1 Selection and Resconstruction

In order to be consistent with charmless decay analysis, we use same final-state particle selection as we used in $B^+ \longrightarrow \omega h^+$ study.

6.1.1 B^+ and $\bar{D}^0$ Resconstriction

We impose a mass-window requirement on the $\bar{D}^0$ candidates, selecting only those whose reconstructed mass lies within the nominal range and discarding any for which the kinematic fit fails to converge. This selection effectively suppresses peaking backgrounds in the low–ΔE region. The subsequent fit is performed over the chosen

doi:10.6342/NTU202504255

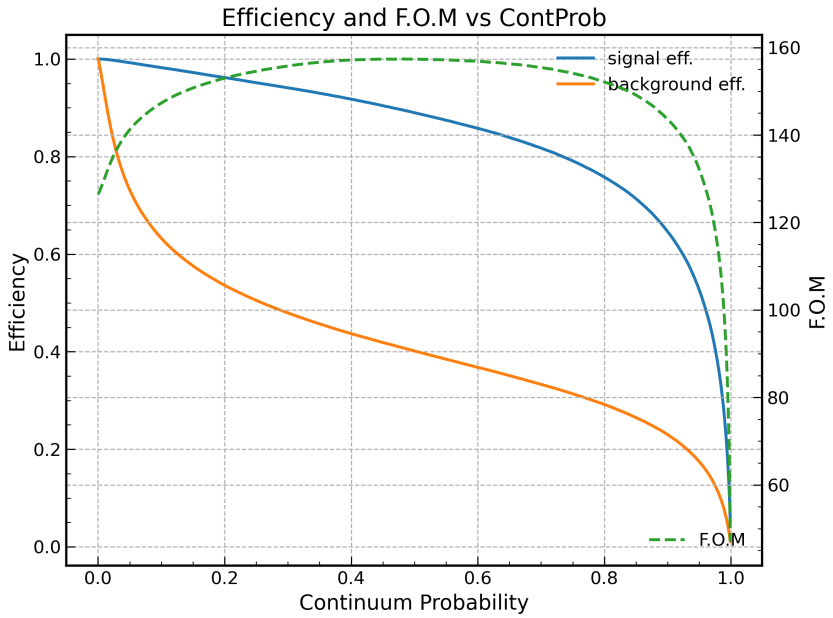

Figure 6.1: Result of The F.O.M of Control Channel with Best CSMVA> 0.48

kinematic range, where $h^{\pm}$ denotes the charged tracks originating from the B and D mesons.

We reconstruct events for two purposes: (a) to extract the shift and scale parameter of the signal and feed across shapes, (b) to assess possible differences in the continuum suppression efficiency between data and simulation.

6.2 Control Sample Modeling and Fitting

We set three fitting componet for the Control Sample: Signal ,$B\bar{B}$background and continuum background. The Modeling details are listed in the Table 6.2

6.3 Fudge Factor

Fudge factors account for the subtle, systematic differences between Monte Carlo simulations and real data that arise from several sources: imperfect modeling of the detector response (e.g. energy calibration and resolution mismatches), variations in reconstruction algorithms (such as tracking and PID threshold settings),

doi:10.6342/NTU202504255

Final state particle selection	
K^+	BinaryKπID >0.6 thetaInCDCAcceptance dr <0.5cm abs(dz) <2cm nCDCHits >20
π^+	BinaryKπID <0.4 thetaInCDCAcceptance dr <0.5cm abs(dz) <2cm nCDCHits >5
γ	clusterE >0.025GeV thetaInCDCAcceptance clusterNHits >1.5 0.2967 <clusterTheta <2.6180 clusterReg=1 for E >0.080GeV clusterReg=2 for E >0.050GeV clusterReg=3 for E >0.060GeV clusterE1E9 <0.9
Reconstructed particle selection	
π^0	abs($\cos\theta_{hel}$) <0.97 0.121 <$M_{\gamma\gamma}$ <0.142GeV
$\bar{D}^0$	1.82GeV <InvM <1.90GeV
B^+	$M_{\rm bc}$ >5.2GeV/c^2 abs(ΔE) <0.25GeV Best candidate : CSMVA Cut>0.48

Table 6.1: Selection criteria for the $B^+ \to \bar{D}^0\pi^+$ ($\bar{D}^0 \to K^+\pi^-\pi^0$) channel.

doi:10.6342/NTU202504255

Table 6.2: Models used for each component in M_{bc} and ΔE.

Component	M_{bc}	ΔE
Continuum background	Argus	Second-order polynomial
$B\bar{B}$ background	Histogram fit	
Signal	Crystal Ball + Gaussian	Double Gaussian

simplifications or omissions in the physics generators (like secondary scattering or beam-energy spread), and time-dependent calibration and alignment shifts present in data but not in simulation. By introducing small shift and scale parameters, fudge factors adjust the simulated shapes to better match the actual data, thereby ensuring more accurate and robust extraction of physics observables.

To evaluate the systematic uncertainty from the fudge factors——the shift and scale parameters between simulation and data—we produce 100 pseudo-datasets by fluctuating the nominal fit shapes within their uncertainties (see Figs. 6.2 and 6.3). Each pseudo-dataset is fitted twice: once with the nominal shapes and once with shapes adjusted by an alternative fudge factor value drawn randomly for that experiment. We then compute the difference between the two fit results for each pseudo-dataset, and take the standard deviation of these 100 differences as the estimated systematic uncertainty.

6.4 FastBDT correction

To suppress the continuum background, we apply a FastBDT classifier trained and validated on simulated samples. Because the shapes of the input-variable distributions in data can differ from those in Monte Carlo, the raw BDT output may be biased when applied to real events. To correct for this, we extract event-by-event calibration weights from dedicated control channels.By comparing the BDT score distributions in data and simulation. These weights are then applied to the classifier output in our signal selection to bring the efficiency in line with true data performance. Finally, we propagate the uncertainty on the ratio of corrected-to-

doi:10.6342/NTU202504255

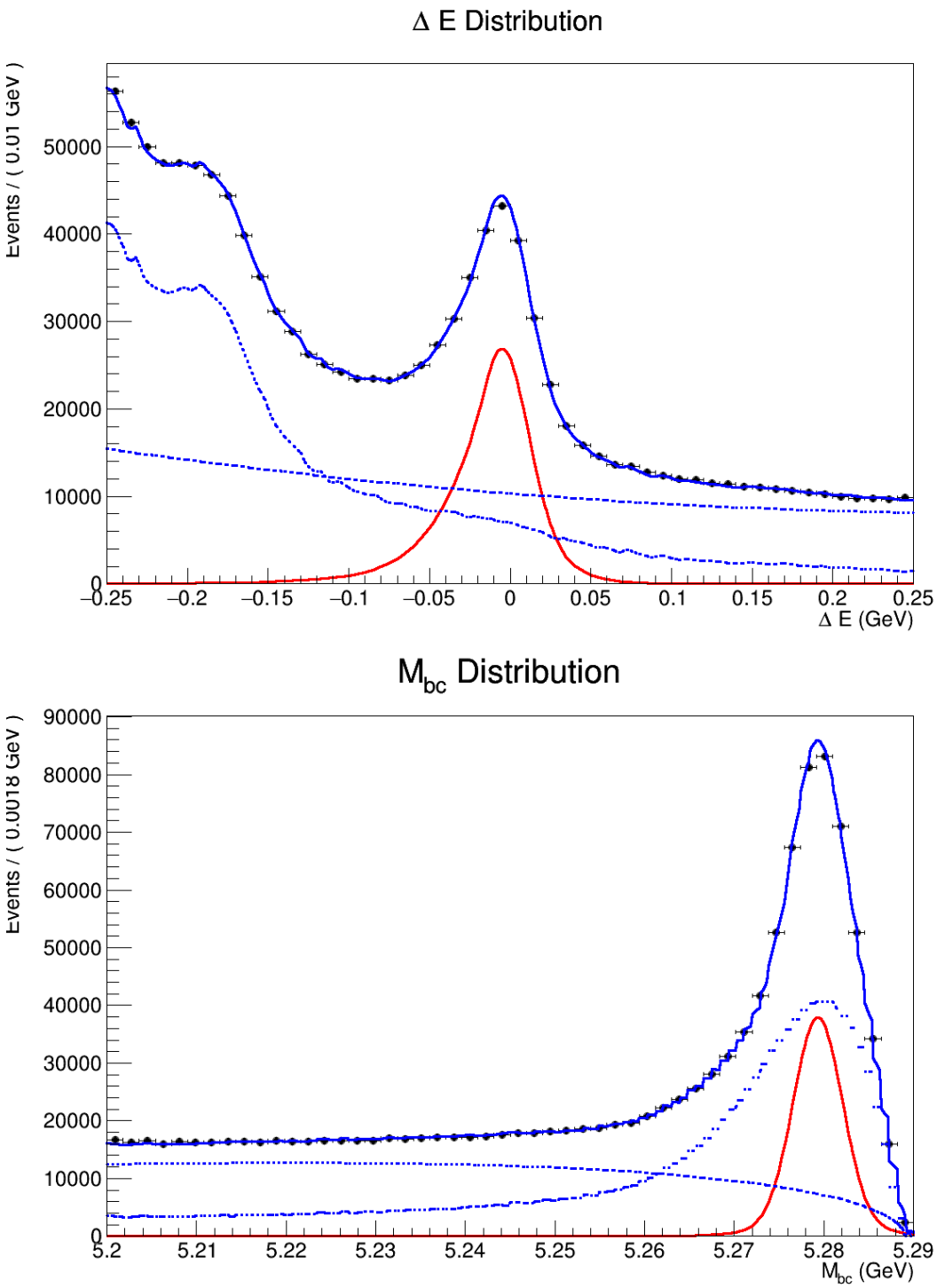

Figure 6.2: Fit projections in Monte Carlo Sample (a) the ΔE distribution and (b) the $M_{\rm bc}$ distribution.

doi:10.6342/NTU202504255

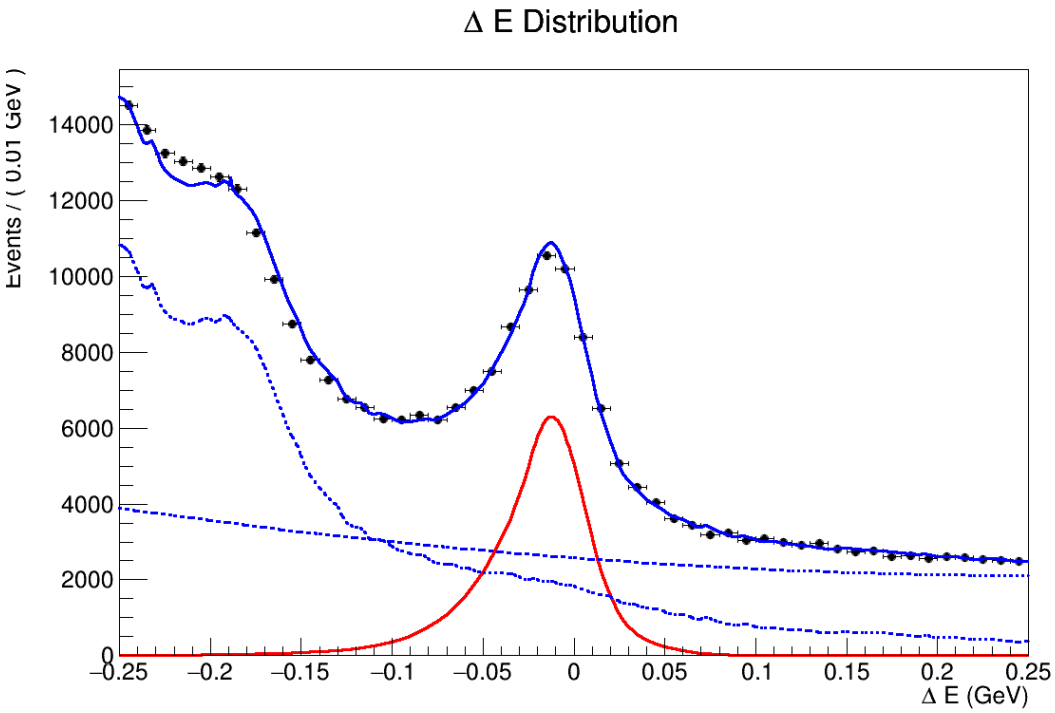

(a) ΔE (data)

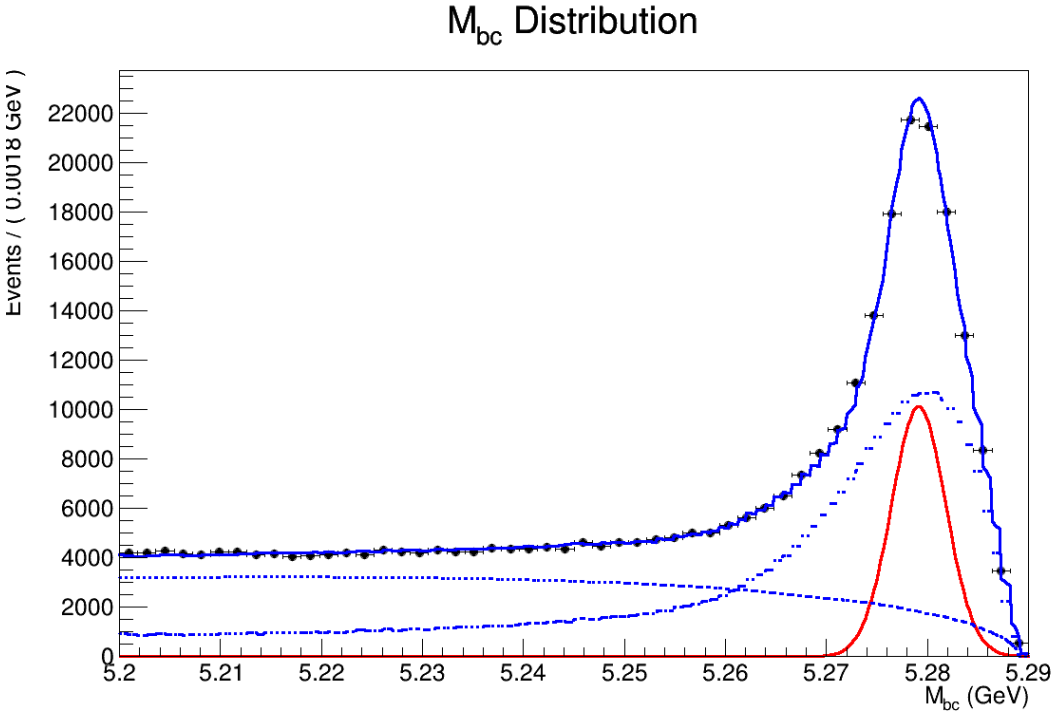

(b) $M_{\rm bc}$ (data)

Figure 6.3: Fit projections to Real data for (a) the ΔE distribution and (b) the $M_{\rm bc}$ distribution.

doi:10.6342/NTU202504255

Table 6.3: Fit results for MC and data: means, widths, branching fractions, mean shifts, and fudge factors. Uncertainties are statistical only.

Category	**Mbc (MeV)**	ΔE **(MeV)**
MC		
Mean	5279.3 ± 0.00977	-5.0479 ± 0.0845
Width	3.171 ± 0.033	20.47 ± 0.15
Br (truth: 4.68×10^{-3})	$(4.65 \pm 0.05) \times 10^{-3}$	
Data		
Mean	5279.1 ± 0.0185	-12.279 ± 0.184
Width	2.733 ± 0.029	22.79 ± 0.34
Br ($(4.53 \pm 0.03) \times 10^{-3}$)	$(4.63 \pm 0.03) \times 10^{-3}$	
Mean shift	-0.20 ± 0.02	-7.23 ± 0.20
Fudge factor	0.862 ± 0.013	1.113 ± 0.018

uncorrected selection efficiencies for each decay mode as a systematic uncertainty in our measurement.

Table 6.4: Continuum suppression (CS) efficiencies.

Sample	**CS efficiency (%)**
Data	76.25 ± 0.31
Simulation	78.67 ± 0.18
Ratio	96.92 ± 0.45

doi:10.6342/NTU202504255

Chapter 7

Systematic Uncertainties

Combine with the Control Sample result , We apply the following Systematic Uncertainties on our measurement.

Table 7.1: Systematic uncertainties for the $\omega K^{\pm}$ and $\omega\pi^{\pm}$ channels on branching fraction (Br) and direct CP asymmetry (A_{CP}).

	$\omega K^{\pm}$		$\omega\pi^{\pm}$	
Source	Br (%)	A_{CP} (%)	Br (%)	A_{CP} (%)
Tracking	0.48	N/A	0.47	N/A
$B\bar{B}$ pair counting	1.50	N/A	1.50	N/A
f_{+-}/f_{00}	2.50	N/A	2.50	N/A
PID	< 0.10	N/A	< 0.10	N/A
FastBDT	1.50	N/A	1.50	N/A
Fudge factor	1.60	0.50	1.50	0.20
Modeling	1.90	0.01	2.50	0.058
π^0 efficiency	19.00	N/A	19.00	N/A
Total	**19.44**	**0.50**	**19.50**	**0.20**

7.1 Tracking

To cover tracking efficiency uncertainties, we assign a 0.48% systematic uncertainty per final-state track on the measured branching fraction. This value is obtained as

doi:10.6342/NTU202504255

follows: **Slow pion tracking efficiency** For "soft π " tracks with momentum in the range 0.05–0.20 GeV, use the Data/MC correction factors and their statistical and systematic uncertainties provided in the three momentum bins (0.05–0.12 GeV, 0.12–0.16 GeV, 0.16–0.20 GeV) on the "Slow pion tracking efficiency" page. [31].

Mid to high momentum tracking efficiency For regular charged particles with momentum $\geq$ 0.20 GeV, apply the recommended per-track systematic uncertainty of 0.27% [31].

For an event with N charged tracks, if the relative uncertainty of the i-th track is σ_i, then the event-level tracking systematic uncertainty is

$$\sigma_{event} = \sqrt{\sum_{i=1}^{N} \sigma_i^2} \tag{7.1}$$

Calculate for all signal events and take the arithmetic mean to obtain the average tracking systematic uncertainty for your signal sample.

7.2 $B\bar{B}$ Pair Counting

We assign a systematic uncertainty of 1.5% to account for the uncertainty of produced BB^{-} pairs according to the performance group[32].

7.3 f_{+-}/f_{00}

The uncertainty on the fraction f_{+-}/f_{00} of $\Upsilon(4S) \to B^+B^-(2.4\%)$ and $BB^-(2.5\%)$ is assigned as systematic uncertainty.

doi:10.6342/NTU202504255

7.4 π_0 and ω Reconstruction efficiency

The efficiency correction for the π^0 reconstruction and selection have been calculated by the neutral group using $D^0 \longrightarrow K^-\pi^+\pi^0$ and $D^0 \longrightarrow K^-\pi^+$ decays [33]. They provided a correction map as a function of the momentum and cosine of polar angle of the π^0. The uncertainty is the sum in quadrature of the statistical and systematic.

7.5 PID correction

The Systematic Correction Framework provides combined statistical and systematic uncertainties for our PID calibration factors. To propagate these into our physics measurements, we perform 500 pseudo-experiments. In each experiment:

1. Generate events using the nominal PDFs and expected component fractions (scaled to the LS1 luminosity), with the total yield fluctuated by a Poisson distribution.

2. Fit the dataset twice: once with default PID corrections and once with corrections varied according to Gaussian uncertainties around their nominal values.

3. Record the difference in each physics observable between the two fits.

We then fit the distribution of these differences with a Gaussian; its width, σ, represents the systematic uncertainty from the PID calibration.

7.6 CS selection

We employ boosted decision tree classifiers, trained and validated on Monte Carlo samples, to reject continuum $q\bar{q}$ background. Discrepancies between data and simulation in the input variable distributions can bias the classifier output. To quantify this, we examine data–MC agreement in dedicated control channels (see Sec. 6.2).

doi:10.6342/NTU202504255

The observed deviation in the efficiency ratio between data and Monte Carlo for each decay mode is assigned as a systematic uncertainty.

7.7 Fudge Factors

We evaluate the systematic uncertainty on the shift and scale ("fudge") parameters by running 100 pseudo-experiments with the nominal fit shapes. Each sample is fitted twice—once with the default parameters and once with those parameters varied randomly within their uncertainties—and the difference between the two results is recorded. The standard deviation of these 100 differences is taken as the systematic uncertainty.

7.8 Modeling

The analytical PDF shapes for signal and feed-across components are obtained from fits to dedicated, high-statistic MC samples, with their parameter uncertainties given by the fit covariance matrix. To quantify the systematic effect of these shape uncertainties, we perform 500 pseudo-experiments for each component. In each trial, events are generated according to the nominal PDF and the expected component fractions derived from generic MC truth scaled to the LS1 integrated luminosity. The total yield in each dataset is fluctuated by drawing from a Poisson distribution around its nominal value. Each toy dataset is then fitted twice: once with the default PDF parameters, and once with parameters randomly varied within their uncertainties (sampling each from a Gaussian centered on its nominal value). We record the difference in the physics observables between the two fits for every pseudo-experiment. Finally, we fit the distribution of these differences with a Gaussian and take its width, σ, as the systematic uncertainty associated with the PDF shape modeling.

doi:10.6342/NTU202504255

Chapter 8

Conclusion

In summary, we have completed the final event-selection procedure using our Monte Carlo (MC) sample and performed a full fit, demonstrating—via the gsim toy-MC tests—that no bias is introduced by our fitting strategy. To assess any residual discrepancies between simulation and reality, we then employed an independent control sample drawn from real data; this study allowed us to quantify data/MC differences and propagate them into our systematic-uncertainty budget.

Combining the control-sample results with a comprehensive evaluation of other sources of systematic error, we assign a total systematic uncertainty of 19.44 % and 19.50%. Going forward, we will further refine and validate each component of this uncertainty estimate in preparation for the unblinding of the real-data sample. These ongoing improvements will ensure the robustness of our final physics measurements. The following fig shows the fitting results in Monte Carlo Sample.

doi:10.6342/NTU202504255

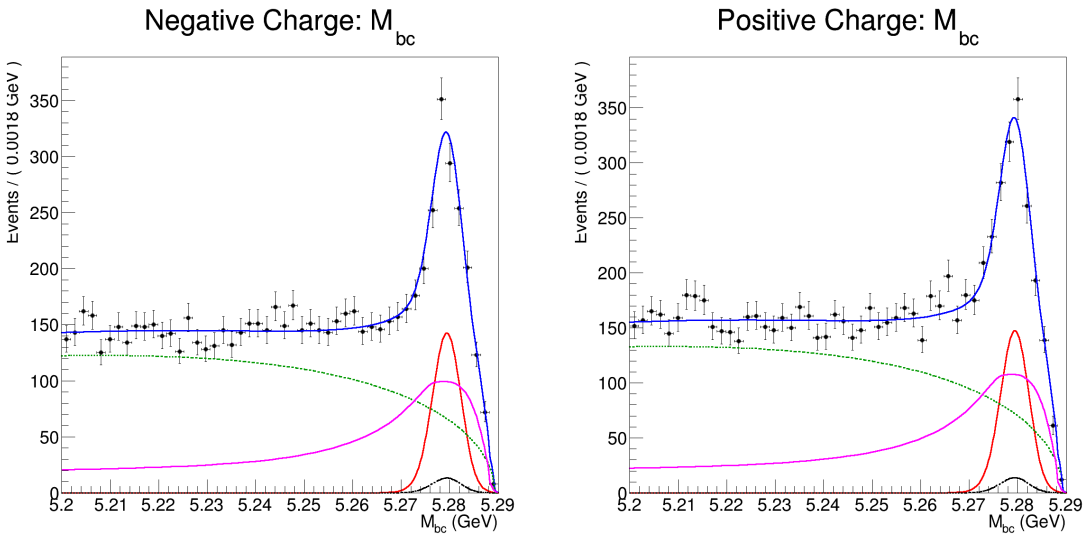

Figure 8.1: ωK^+ Mbc

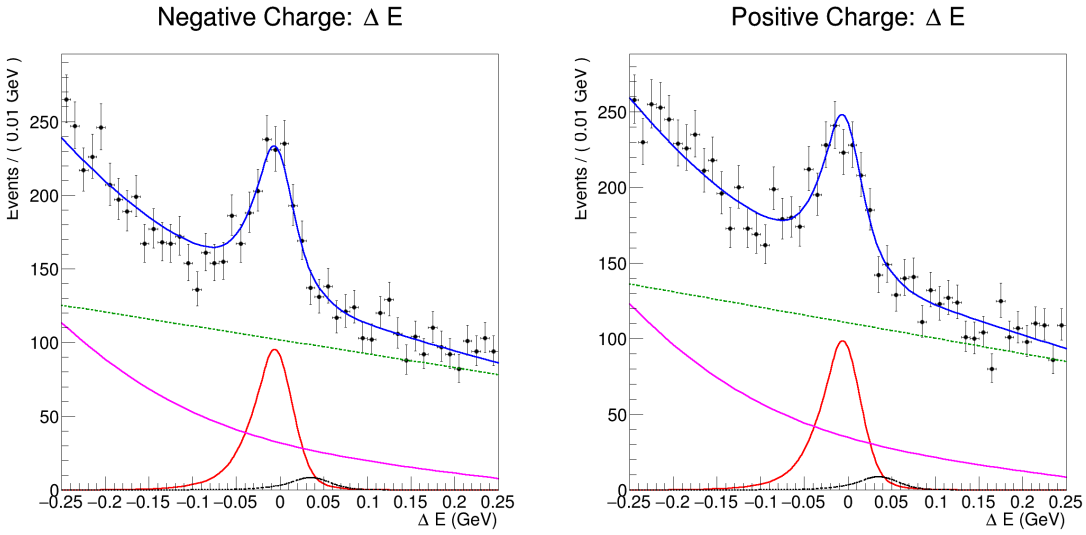

Figure 8.2: ωK^+ ΔE

doi:10.6342/NTU202504255

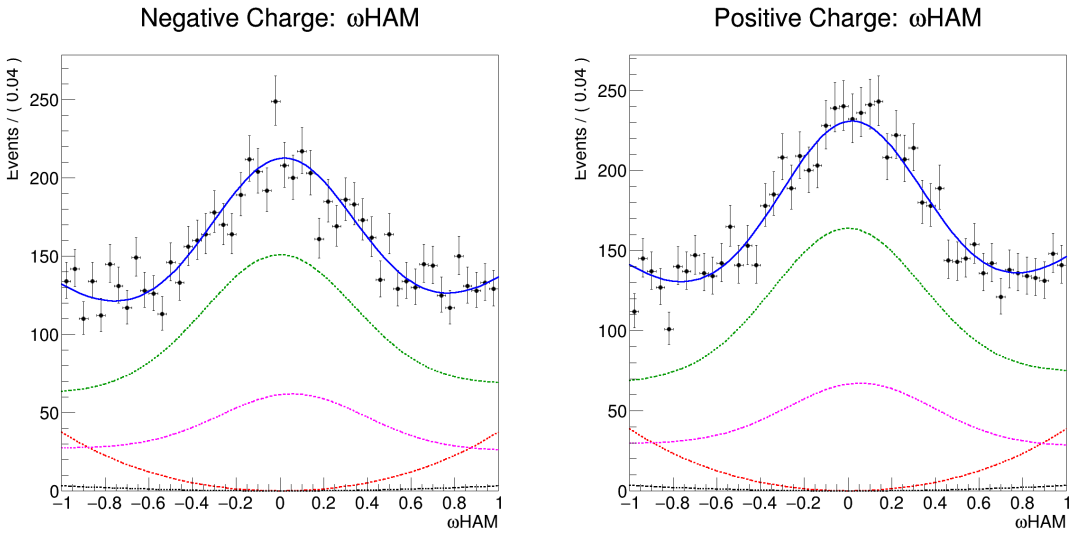

Figure 8.3: ωK^+ $\mathcal{H}_{3\pi}$

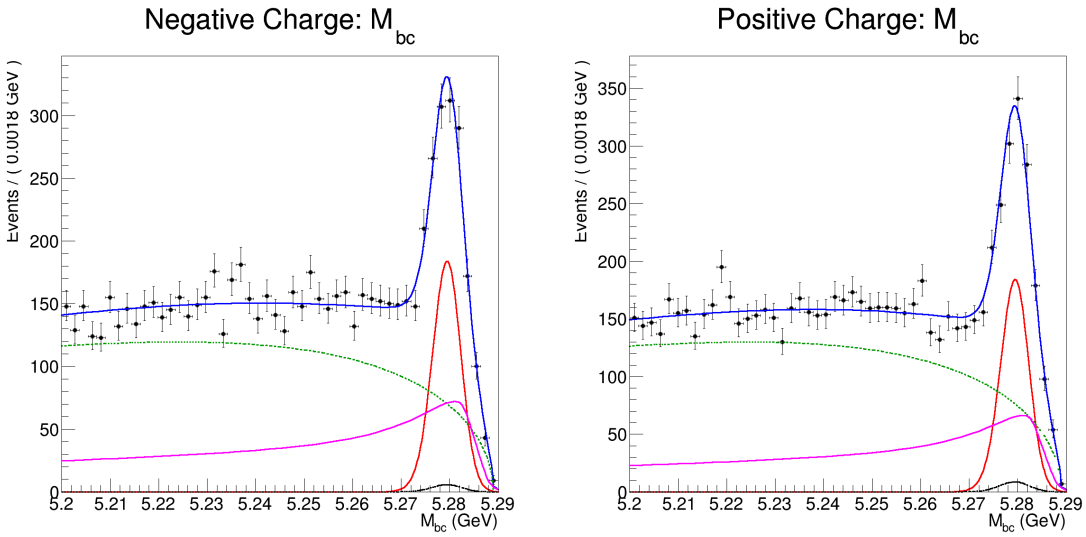

Figure 8.4: $\omega\pi^+$ Mbc

doi:10.6342/NTU202504255

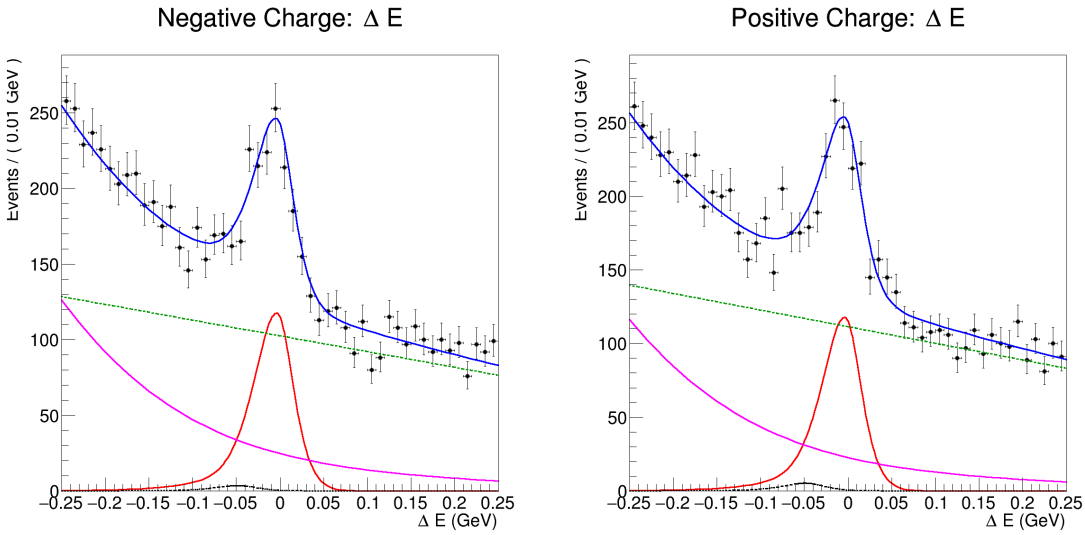

Figure 8.5: $\omega\pi^+$ ΔE

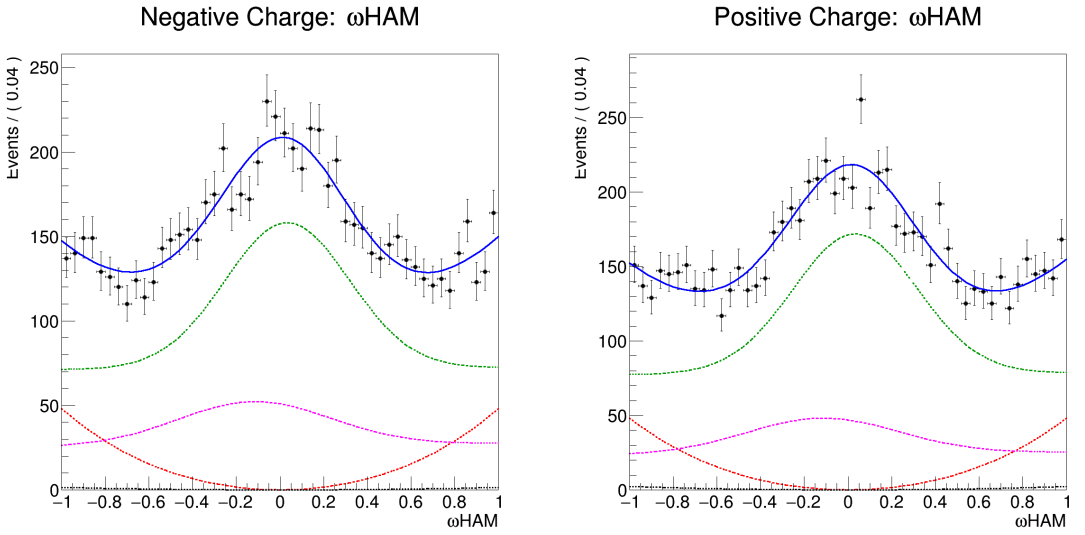

Figure 8.6: $\omega\pi^+$ $\mathcal{H}_{3\pi}$

doi:10.6342/NTU202504255

Bibliography

[1] A. D. Sakharov. Violation of cp invariance, c asymmetry, and baryon asymmetry of the universe. *Sov. Phys. Usp.*, 34:392, 1991.

[2] N. Cabibbo. Unitary symmetry and leptonic decays. *Physical Review Letters*, 10:531, 1963.

[3] M. Kobayashi and T. Maskawa. Cp-violation in the renormalizable theory of weak interaction. *Progress of Theoretical Physics*, 49:652, 1973.

[4] S. L. Glashow, J. Iliopoulos, and L. Maiani. Weak interactions with lepton–hadron symmetry. *Physical Review D*, 2:1285, 1970.

[5] Hai-Yang Cheng and Chun-Khiang Chua. Title unknown. *Phys. Rev. D*, 80:114008, 2009.

[6] Hsiang-Nan Li and Satoshi Mishima. Title unknown. *Phys. Rev. D*, 74:094020, 2006.

[7] Wei Wang, Yu-Ming Wang, De-Shan Yang, and Cai-Dian Lü. Title unknown. *Phys. Rev. D*, 78:034011, 2008.

[8] V. Chobanova, J. Dalseno, C. Kiesling, I. Adachi, H. Aihara, D. M. Asner, V. Aulchenko, T. Aushev, T. Aziz, A. M. Bakich, and ... (Belle Collaboration). Measurement of branching fractions and cp violation parameters in $b \to \omega k$ decays with first evidence of cp violation in $b^0 \to \omega k_s^0$. *Physical Review D*, 90:012002, 2014.

doi:10.6342/NTU202504255

[9] B. Aubert and et al. Measurements of cp-violating asymmetries and branching fractions in b decays to ωk and $\omega\pi$. *Phys. Rev. D*, 74(1):011106(R), 2006.

[10] E. Kou et al. The belle ii physics book. *Prog. Theor. Exp. Phys.*, page 123C01, 2019. (Belle II Collaboration).

[11] A. J. Bevan et al. The physics of the b factories. *Eur. Phys. J. C*, 74:3026, 2014.

[12] Y. Ohnishi et al. Accelerator design at superkekb. *Prog. Theor. Exp. Phys.*, page 03A011, 2013.

[13] M. Akatsu et al. Title unknown. *Nucl. Instrum. Meth.*, A440:124–135, 2000. arXiv:physics/9904009.

[14] J. Kemmer et al. Title unknown. *Nucl. Instrum. Meth.*, A253:378–381, 1987.

[15] P. Fischer et al. Title unknown. *Nucl. Instrum. Meth.*, A582:843–848, 2007.

[16] T. Abe. Belle ii. `https://arxiv.org/abs/1011.0352`, 2010. arXiv:1011.0352.

[17] T. Aushev and et al. A scintillator based muon and K_L^0 detector for the Belle II experiment, 2014.

[18] S. Longo, J. M. Roney, C. Cecchi, S. Cunliffe, T. Ferber, H. Hayashii, C. Hearty, A. Hershenhorn, A. Kuzmin, E. Manoni, F. Meier, K. Miyabayashi, I. Nakamura, M. Remnev, A. Sibidanov, Y. Unno, Y. Usov, and V. Zhulanov. CsI(Tl) Pulse Shape Discrimination with the Belle II Electromagnetic Calorimeter as a Novel Method to Improve Particle Identification at Electron-Positron Colliders. *J. Instrum.*, 15(C0016):1–23, 2020.

[19] Belle II Collaboration. Electromagnetic Calorimeter. Belle II Experiment website, 2023.

doi:10.6342/NTU202504255

[20] Z. Dolezal and S. Uno. Belle II Technical Design Report. KEK Report 2010-1, KEK, 2010. Department of Physics, University of Hawaii.

[21] S. Bähr and et al. The neural network first-level hardware track trigger of Belle II. *Nucl. Instrum. Meth. A*, 2025. Submitted; available on ScienceDirect.

[22] E. Won, J. B. Kim, and B. R. Ko. Three dimensional fast tracker for central drift chamber based level 1 trigger system in the Belle II experiment, 2017.

[23] M. Nakao and et al. Performance of the Unified Readout System of Belle II, 2020.

[24] R. Itoh and et al. The Performance of Belle II High Level Trigger in the First Physics Runs. In *EPJ Web Conf. CHEP2020*, volume 245, page 01040, 2020.

[25] N. Braun and T. Kuhr. Software for Online Reconstruction and Filtering at the Belle II Experiment, 2020.

[26] Belle II Collaboration. High-Level Trigger (HLT): Software trigger. Overview of the Belle II High Level Trigger, USTC Indico, Nov. 21, 2024, 2024. Online presentation.

[27] F. Abudinén and II Collaboration Belle˙ B-flavor tagging at belle ii. *European Physical Journal C*, 82:283, 2022.

[28] G. C. Fox and S. Wolfram. Observables for the analysis of event shapes in e^+e^- annihilation and other processes. *Physical Review Letters*, 41:1581, 1978.

[29] A. Abashian and et al. The Belle Detector. *Nucl. Instrum. Meth. A*, 479:117–232, 2002. Section 4.5 details continuum suppression and Fox–Wolfram moments.

[30] K. Abe and et al. Measurement of Time-Dependent CP-Violating Asymmetries in $B^0 \to J/\psi K^0_S$ Decays. *Phys. Rev. D*, 66:032007, 2002.

doi:10.6342/NTU202504255

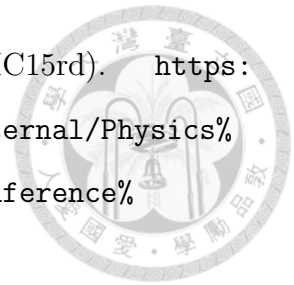

[31] Belle II Collaboration. Conference readiness (until MC15rd). https://xwiki.desy.de/xwiki/bin/view/BI/Belle%20II%20Internal/Physics%20Performance%20Webhome/Conference%20readiness/Conference%20readiness%20%28until%20MC15rd%29/, 2025.

[32] Belle II Collaboration. Belle II Physics Public Note: Measurement of the energy dependence of the $e^+e- \longrightarrow B\bar{B}, B\bar{B}^*$ and $B^*\bar{B}^*$ cross sections at Belle II. Belle II Physics Public Note BELLE2-PUB-PH-2023-016, Belle II Collaboration, 2023.

[33] Neutral Reconstruction Performance Group. π^0 Reconstruction Efficiency Calibration using $D^0 \to K^-\pi^+\pi^0$ and $D^0 \to K^-\pi^+$ Decays. Belle II Internal Note BELLE2-NOTE-PERF-2025-001, Belle II Collaboration, 2025. Belle II Internal Note.

doi:10.6342/NTU202504255

Appendices

doi:10.6342/NTU202504255

Appendix A

ω Meson Helicity Distribution

The ωmeson is a spin-1 (vector) particle. Its decay amplitude to $\pi^+\pi^-\pi^0$ is proportional to the dot product of its polarization vector $\boldsymbol{\varepsilon}$ and the normal $\mathbf{n}$ to the three-pion decay plane:

$$\mathcal{M} \propto \boldsymbol{\varepsilon} \cdot \mathbf{n}\,.$$

Averaging over the three polarization states using

$$\sum_{\lambda} \varepsilon_i^{(\lambda)} \varepsilon_j^{*(\lambda)} = \delta_{ij} - \hat{p}_i \hat{p}_j$$

gives

$$\langle |\mathcal{M}|^2 \rangle \;\propto\; 1 - \cos^2\theta_H, \quad \cos\theta_H = \frac{\boldsymbol{\varepsilon} \cdot \mathbf{n}}{|\boldsymbol{\varepsilon}||\mathbf{n}|}\,.$$

Including the three-body phase-space Jacobian, which also contributes a factor of $(1 - \cos^2\theta_H)$, yields the helicity distribution

$$\frac{d\Gamma}{d\cos\theta_H} \;\propto\; (1 - \cos^2\theta_H)^2 \;=\; 1 - 2\cos^2\theta_H + \cos^4\theta_H.$$

This is a symmetric quartic polynomial in $\cos\theta_H$, invariant under $\cos\theta_H \to -\cos\theta_H$.

doi:10.6342/NTU202504255

Appendix B

Distribution of Training Variables

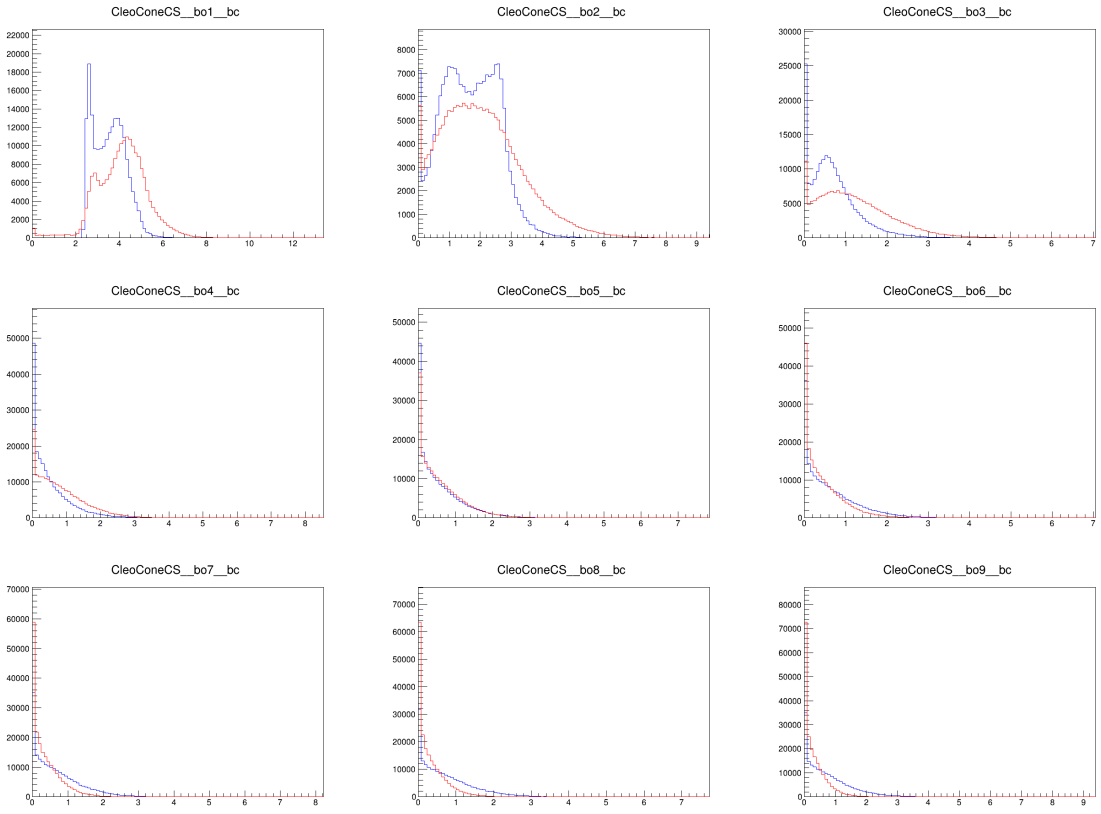

Figure B.1: Input variable distributions used for training the continuum-suppression classifier. Each plot shows normalized shapes for signal vs. background.

doi:10.6342/NTU202504255

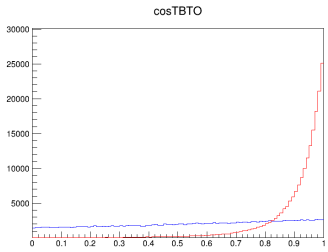

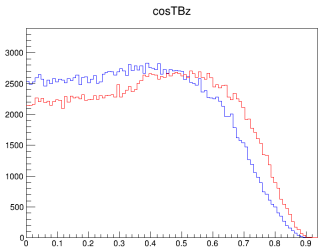

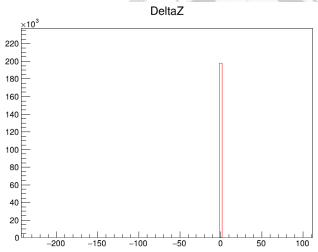

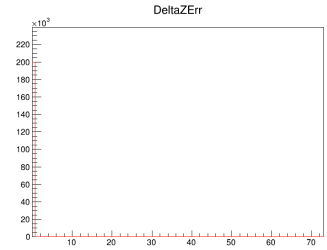

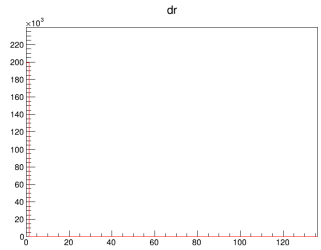

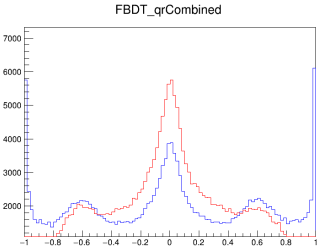

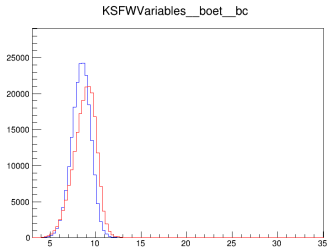

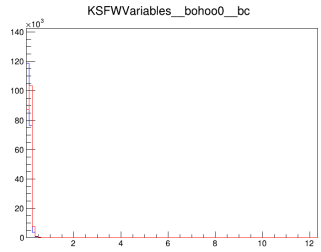

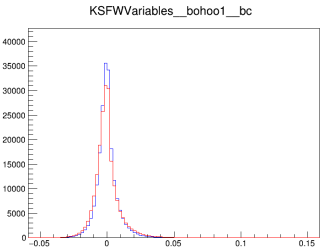

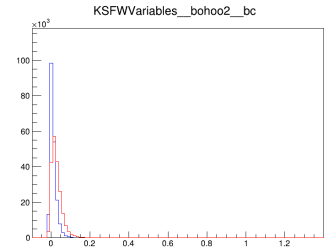

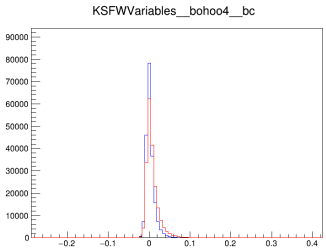

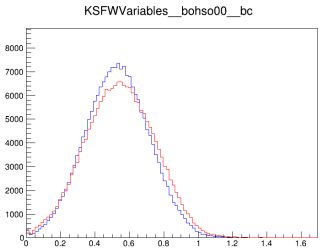

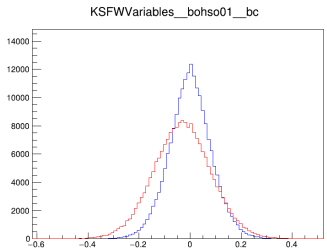

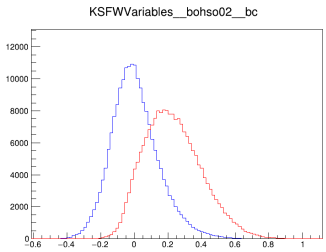

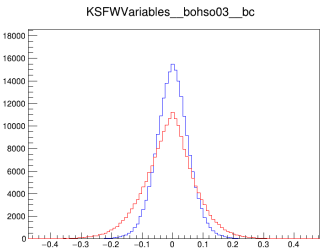

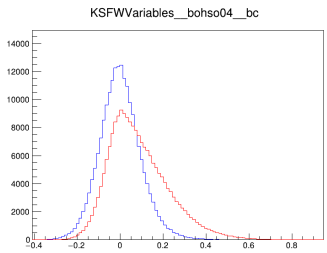

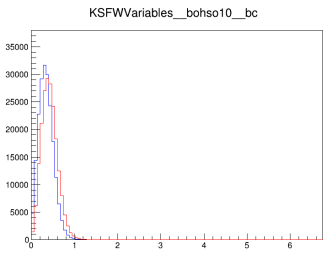

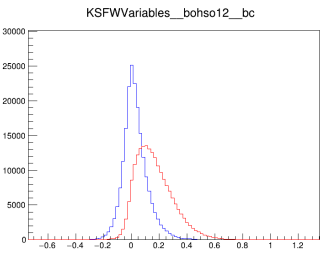

doi:10.6342/NTU202504255

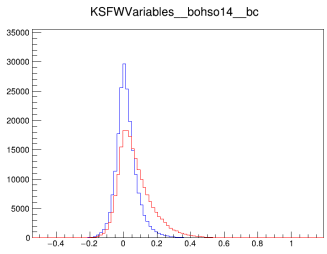

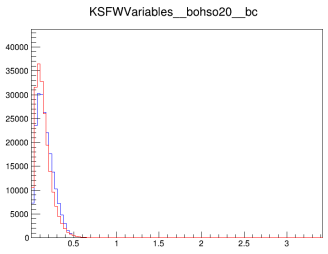

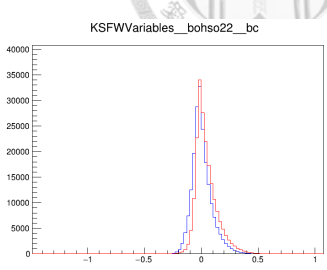

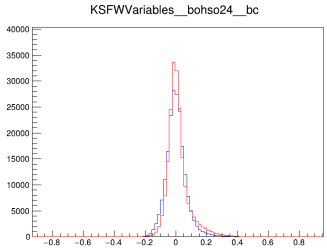

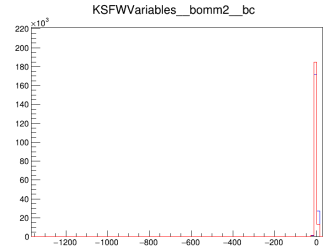

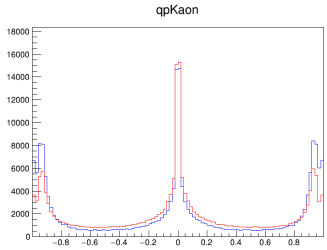

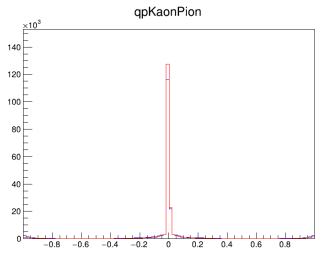

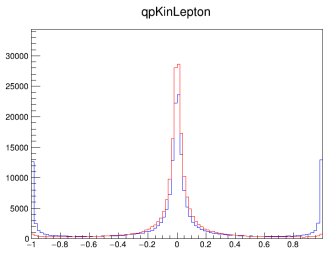

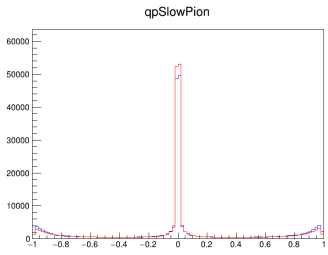

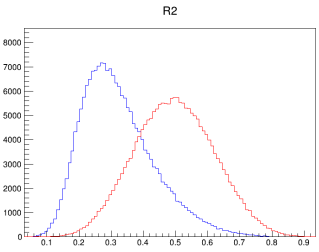

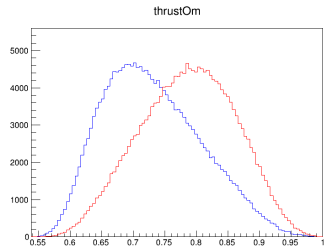

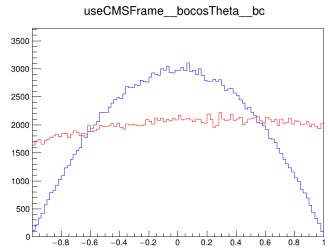

doi:10.6342/NTU202504255

Appendix C

Pdf Modeling

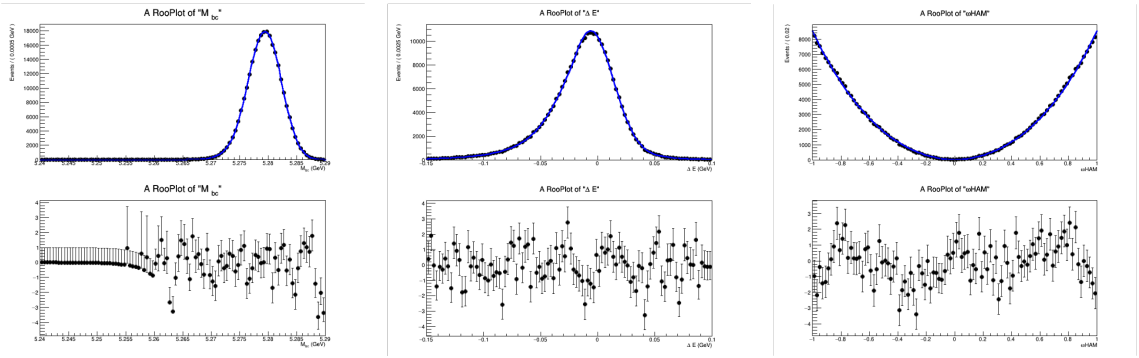

Figure C.1: Signal Model for ωK^+

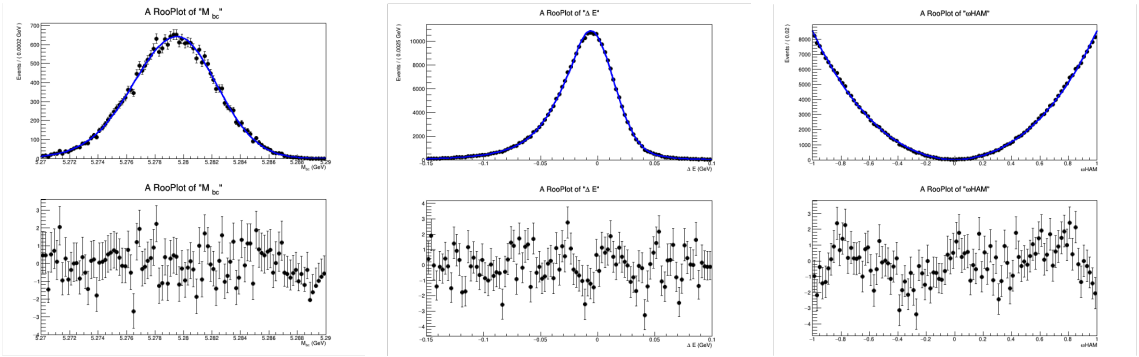

Figure C.2: Feed Across Model for ωK^+

doi:10.6342/NTU202504255

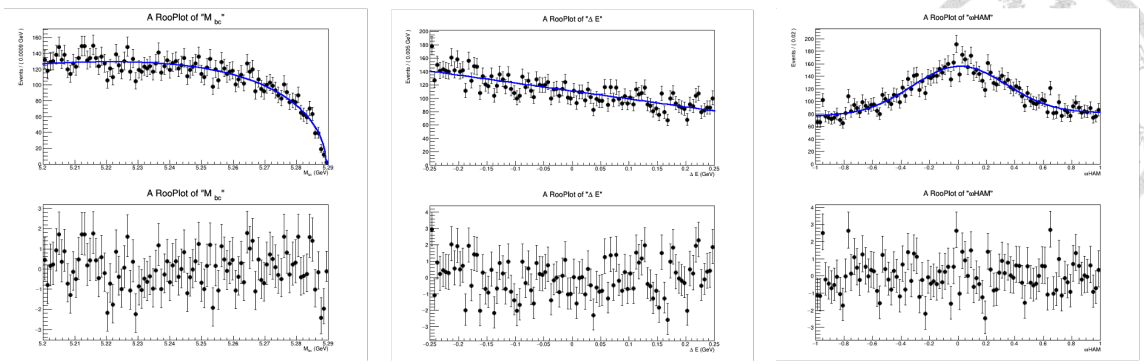

Figure C.3: Continuum background Model for ωK^+

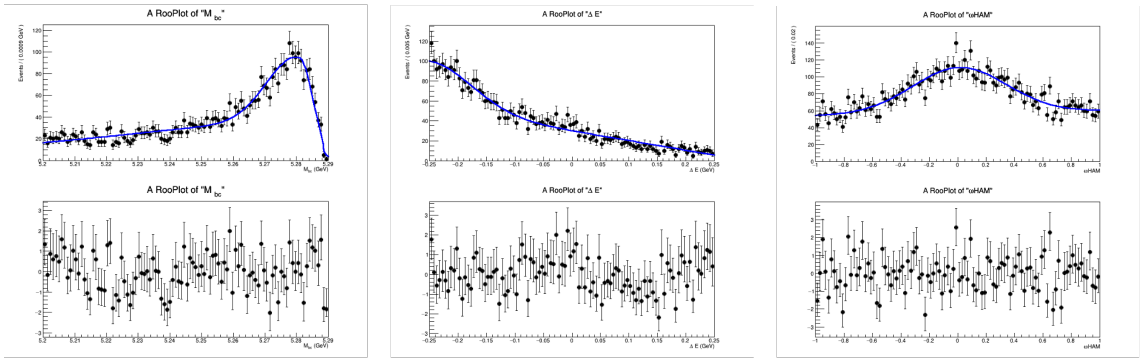

Figure C.4: BB background Model for ωK^+

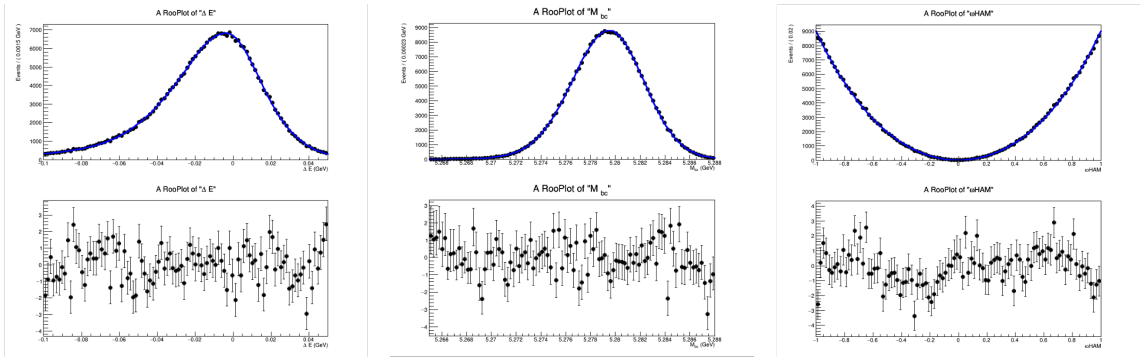

Figure C.5: signal model for $\omega\pi^+$

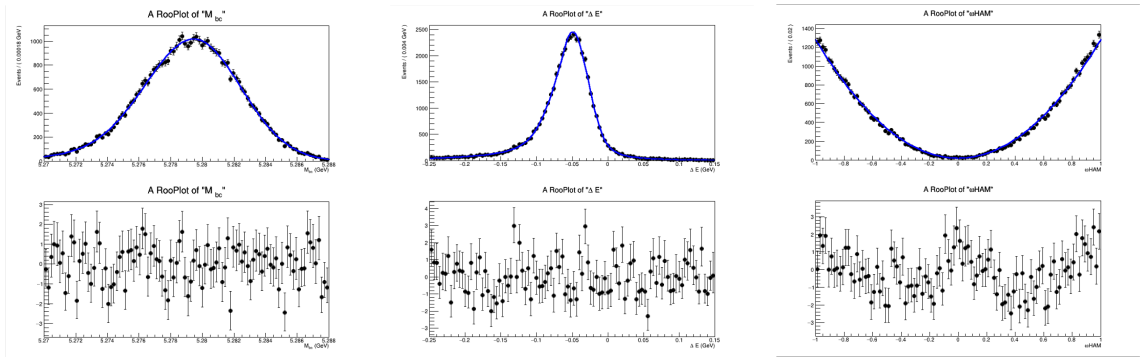

Figure C.6: Feed across Model for $\omega\pi^+$

doi:10.6342/NTU202504255

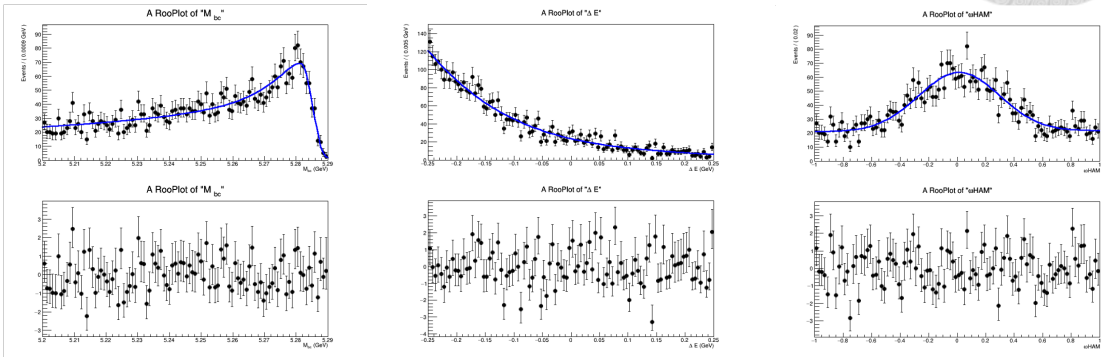

Figure C.7: bb background Model for $\omega\pi^+$

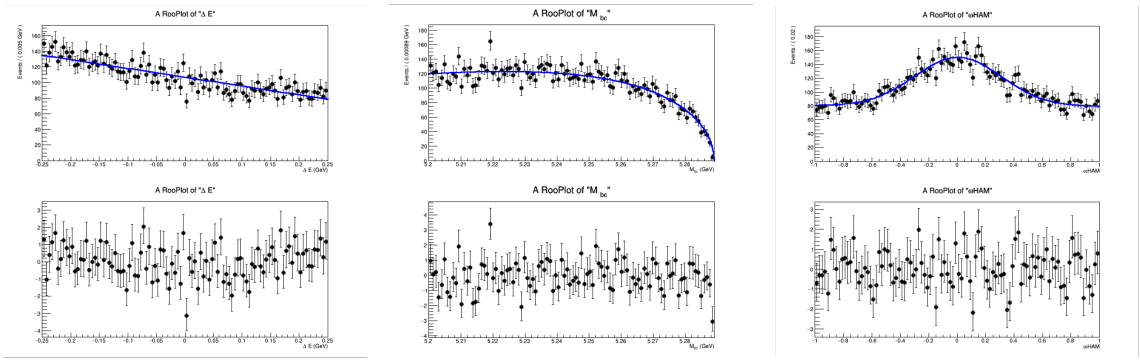

Figure C.8: continuum background Model for $\omega\pi^+$

doi:10.6342/NTU202504255

Appendix D

Correlation of Fitting Component

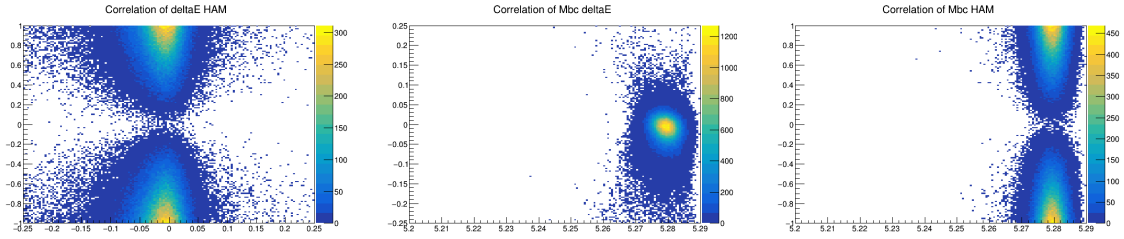

(a) (b) (c)

Figure D.1: Signal PDF correlation plots.

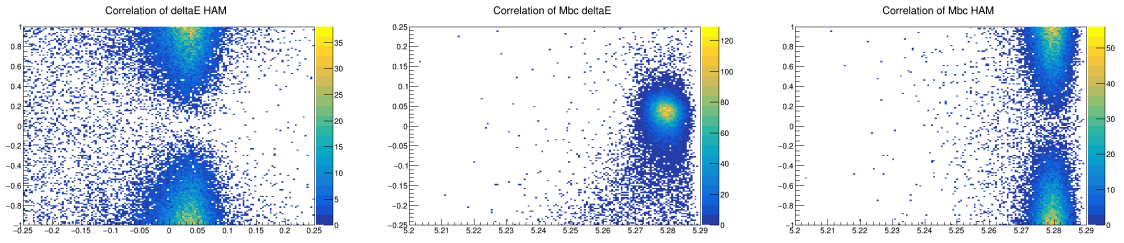

(a) (b) (c)

Figure D.2: Feed-across PDF correlation plots.

doi:10.6342/NTU202504255

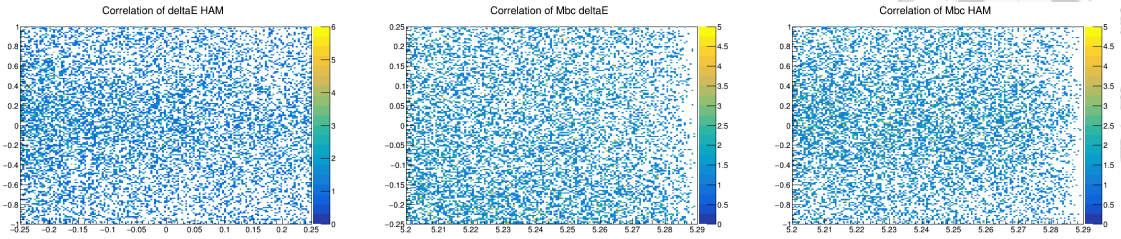

(a) (b) (c)

Figure D.3: Continuum (qq) PDF correlation plots.

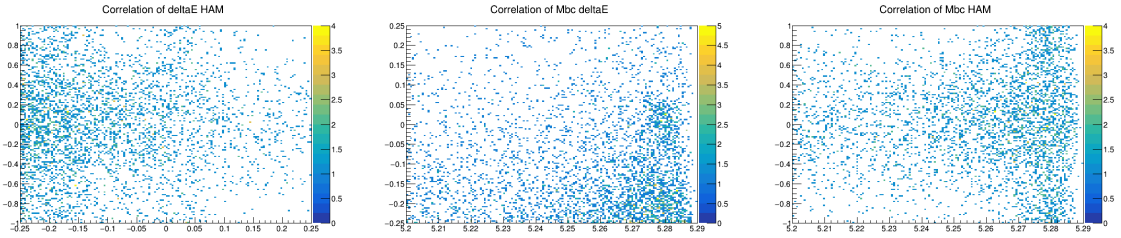

(a) (b) (c)

Figure D.4: BB-background PDF correlation plots.

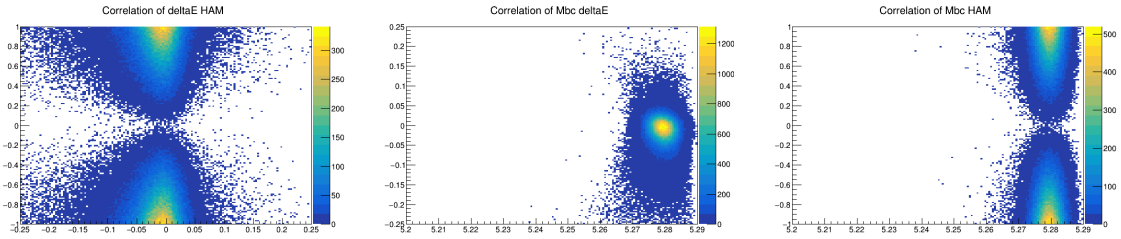

Figure D.5: Signal PDF correlation plots: (a) ΔE vs. $\mathcal{H}_\omega$, (b) $M_{\rm bc}$ vs. ΔE, (c) $M_{\rm bc}$ vs. $\mathcal{H}_\omega$.

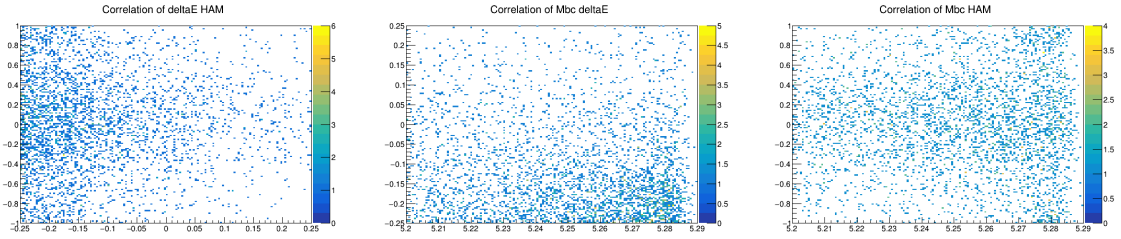

Figure D.6: BB-background PDF correlation plots: (a) ΔE vs. $\mathcal{H}_\omega$, (b) $M_{\rm bc}$ vs. ΔE, (c) $M_{\rm bc}$ vs. $\mathcal{H}_\omega$.

doi:10.6342/NTU202504255

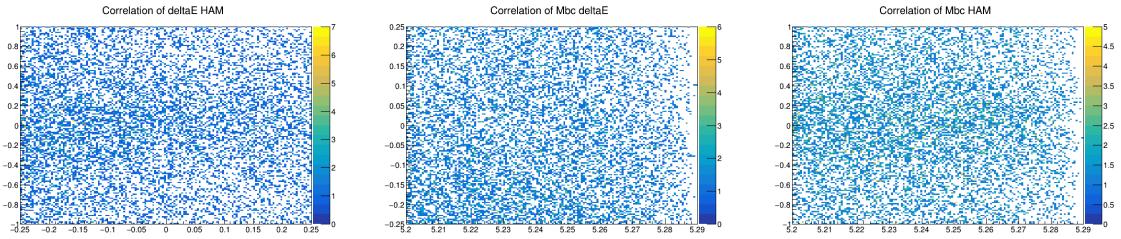

Figure D.7: Continuum (qq) PDF correlation plots: (a) ΔE vs. $\mathcal{H}_\omega$, (b) $M_{\rm bc}$ vs. ΔE, (c) $M_{\rm bc}$ vs. $\mathcal{H}_\omega$.

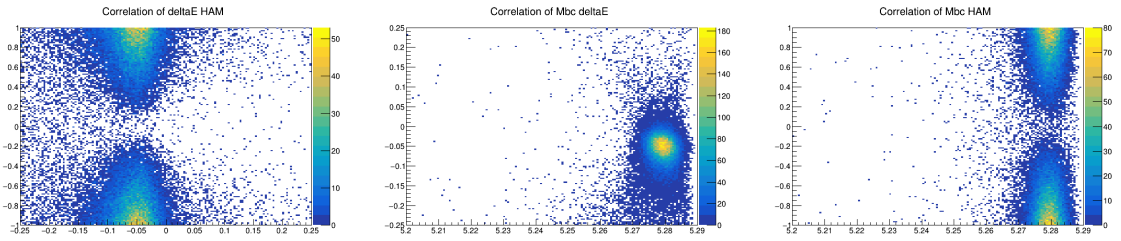

Figure D.8: Feed-across PDF correlation plots: (a) ΔE vs. $\mathcal{H}_\omega$, (b) $M_{\rm bc}$ vs. ΔE, (c) $M_{\rm bc}$ vs. $\mathcal{H}_\omega$.

doi:10.6342/NTU202504255